



Modeling diffusion-governed solidification of ternary alloys – Part 2: Macroscopic transport phenomena and macrosegregation



M. Wu^{a,b,*}, J. Li^{a,b}, A. Ludwig^b, A. Kharicha^{a,b}

^a Christian Doppler Laboratory for Advanced Process Simulation of Solidification and Melting, University of Leoben, A-8700 Leoben, Austria

^b Department of Metallurgy, University of Leoben, A-8700 Leoben, Austria

ARTICLE INFO

Article history:

Received 13 November 2013

Received in revised form 14 May 2014

Accepted 15 May 2014

Keywords:

Microsegregation

Solidification

Macrosegregation

Ternary alloy

Steel ingot

ABSTRACT

Part 1 of this two-part investigation presented a multiphase solidification model incorporating the finite diffusion kinetics and ternary phase diagram with the macroscopic transport phenomena (Wu et al., 2013). In Part 2, the importance of proper treatment of the finite diffusion kinetics in the calculation of macrosegregation is addressed. Calculations for a two-dimensional (2D) square casting ($50 \times 50 \text{ mm}^2$) of Fe–0.45 wt.%C–1.06 wt.%Mn considering thermo-solutal convection and crystal sedimentation are performed. The modeling result indicates that the infinite liquid mixing kinetics as assumed by classical models (e.g., the Gulliver–Scheil or lever rule), which cannot properly consider the solute enrichment of the interdendritic or inter-granular melt at the early stage of solidification, might lead to an erroneous estimation of the macrosegregation. To confirm this statement, further theoretical and experimental evaluations are desired. The pattern and intensity of the flow and crystal sedimentation are dependent on the crystal morphologies (columnar or equiaxed); hence, the potential error of the calculated macrosegregation caused by the assumed growth kinetics depends on the crystal morphology. Finally, an illustrative simulation of an engineering 2.45-ton steel ingot is performed, and the results are compared with experimental results. This example demonstrates the model applicability for engineering castings regarding both the calculation efficiency and functionality.

© 2014 The Authors. Published by Elsevier B.V. This is an open access article under the CC BY-NC-ND license (<http://creativecommons.org/licenses/by-nc-nd/3.0/>).

1. Introduction

Part 1 of this two-part investigation presented a multiphase solidification model that incorporated the finite diffusion kinetics and ternary phase diagram with the macroscopic transport phenomena [1], and this model was used to analyze the solidification of a ternary alloy (Fe–0.45 wt.%C–1.06 wt.%Mn) for cases without flow. The finite diffusion kinetics in both the liquid and solid were observed to play an important role in the formation of the microsegregation and solidification path, especially at the initial stage of solidification. Under normal casting conditions (where the cooling rate is not too high), the finite diffusion in the solid was recognized as an important phenomenon governing the solidification path [2]; however, the importance of finite diffusion in the liquid has not been paid sufficient attention because for most technical alloys, the diffusion coefficient of the liquid is 2 to 3 orders of magnitude larger than that of the solid. Researchers normally believe that the liquid can be treated as infinite mixing; hence, models

such as the lever rule, Gulliver–Scheil, Brody–Flemings [3], and Clyne–Kurz [4] are valid for analyzing the solidification path. In Part 1, we compared the solidification paths ($T - f_s$ curve and path of $(c_{\ell, \text{Mn}}, c_{\ell, \text{C}})$, etc.) predicted by the models considering different liquid diffusion kinetics and observed that with the assumption of infinite-mixing in the liquid (Gulliver–Scheil or lever rule), it was not possible to model the initial solidification stage adequately [1]. In ternary (or multicomponent) systems, the diffusion of each individual element in the liquid plays an even more important role. Due to the large difference between the two solute elements (C and Mn) in the diffusion coefficient, partition coefficient, and liquidus slope, there is initially almost no enrichment of Mn in the liquid, while the liquid concentration of C is progressively enriched. The difference between the equilibrium concentration ($c_{\ell, i}^*$) and volume-averaged concentration ($c_{\ell, i}$) of the interdendritic or inter-granular melt is significant at the initial stage of solidification. The assumption of $c_{\ell, i}^* = c_{\ell, i}$ by the infinite liquid mixing kinetics does not apply at this initial stage. This phenomenon has actually been recognized for decades [2,5–7]; however, the numerical treatment of the finite diffusion kinetics and its importance in the calculation of macrosegregation have not been systematically investigated.

* Corresponding author at: Department of Metallurgy, University of Leoben, A-8700 Leoben, Austria. Tel.: +43 38424023103.

E-mail address: menghuai.wu@unileoben.ac.at (M. Wu).

It is understood that macrosegregation occurs due to relative motion between the liquid and solid, resulting from different interdendritic/inter-granular flow and crystal sedimentation phenomena [8,9]. The early stage of solidification appears to be the most critical for the formation of macrosegregation because the significant interdendritic/inter-granular flow and crystal sedimentation phenomena occur at this stage. At the late stage of solidification, as the dendrite network is developed in the deep mushy zone or the equiaxed crystals are densely packed, flow becomes less significant.

Most solidification models applicable for the calculation of macrosegregation are based on a predefined solidification path in accordance with the lever rule assumption [10–17], the Gulliver–Scheil assumption [15–23], or an assumption of infinite solute mixing in the liquid combined with finite solid back diffusion [24–28]. A comparison study (lever rule against Gulliver–Scheil) by Schneider and Beckermann [15] for the case of solidification considering only thermo-solutal convection indicated no significant difference in the calculation of macrosegregation. In contrast, a similar comparison by Sundarraj and Voller [28] for another case considering shrinkage-induced flow during solidification indicated a strong difference in the calculation of inverse segregation between the lever rule and Gulliver–Scheil. A common base of all of the aforementioned models is the assumption of infinite solute mixing in the liquid. Only limited studies have been performed [28–30] that have attempted to incorporate the finite diffusion kinetics in the liquid with the macrosegregation models; however, all of these studies were limited to the binary alloy system and made no distinction (or comparison) between cases of different crystal morphologies (columnar, equiaxed, and mixed columnar–equiaxed).

The first volume-average-based model incorporating diffusion growth kinetics, which considers the multiphase nature, was developed by Beckermann et al. [31,32]. This model was recently extended by the current authors to include the mixed columnar–equiaxed solidification for ternary alloys [1]. The morphology of the growing crystals is simplified: a cylinder for columnar and a sphere for equiaxed, such that the diffusion-governed growth kinetics around and inside the growing crystals can be solved analytically. The main advantage of this simplification is to enhance the calculation efficiency, as the computational cost of most macrosegregation models is very high.

Models including both diffusion growth kinetics and dendritic morphology are also available. Significant advances were made with the contributions of Rappaz and Thevoz [5,6] who proposed a micro–macro solute diffusion model for equiaxed dendritic solidification. Following this work, Wang and Beckermann [33–35] suggested a multiphase approach encompassing either equiaxed or columnar solidification, in which a volume-averaging method was used to model multiphase transport phenomena including flow and grain sedimentation. Recently, Ciobanas and Fautrelle [36,37] proposed an ensemble-averaged multiphase Eulerian model for mixed columnar–equiaxed solidification, although convection and grain sedimentation were not considered. Rappaz and Boettinger [7] extended the model of Rappaz and Thevoz to consider the ternary alloy, and the model was used to analyze the effect of various diffusion coefficients of the solute elements on the solidification path. Building upon the major features of these works, an expanded model (for binary alloys), which encompasses mixed equiaxed–columnar solidification, convection, and grain sedimentation and tracks the evolution of dendritic morphologies has been presented by the current authors [38–41]. Although some trials were made using such a model for calculating macrosegregation [42], the high calculation cost has prevented the model from being applied recently for calculations of engineering castings.

Additionally, some morphological parameters describing the crystal envelope need to be determined and validated in advance.

In the current paper (Part 2), parameter studies on the same 2D square casting ($50 \times 50 \text{ mm}^2$) of Fe–0.45 wt.%C–1.06 wt.%Mn as described in Part 1 [1] are performed, and melt flow and crystal sedimentation are considered. The study examines the liquid diffusion kinetics (finite diffusion against infinite diffusion) and its effect on the formation of macrosegregation.

2. Numerical model and simulation settings

A mixed columnar–equiaxed solidification model was presented previously [43,44], and this model was extended to consider ternary alloys [1,45,46]. The key features of the model include:

1. Three phases are considered: liquid (ℓ), equiaxed (e), and columnar (c). These phases are quantified by their volume fractions: f_ℓ , f_e , and f_c , respectively. Simple crystal morphologies are assumed: spheres for equiaxed (globular) grains and cylinders for columnar (cellular) dendrite trunks.
2. The solidification (mass transfer) rate is calculated by considering the growth of the equiaxed crystals and columnar trunks based on the finite diffusion-governed growth kinetics. Thermodynamic equilibrium is primarily assumed at the solid–liquid interface, and solute partitioning occurs at the interface during solidification. $c_{\ell,i}^*$, $c_{e,i}^*$ and $c_{c,i}^*$ represent the thermodynamic equilibrium concentrations at the interface. The volume-averaged concentrations of different phases are numerically solved: $c_{\ell,i}$, $c_{e,i}$, $c_{c,i}$, where $i = A$ or B , representing different solute elements. The growth velocity of the crystal is derived based on a Stefan problem at the interface by solving the diffusion fields around and inside the crystals (cylinder or sphere) analytically [1]. The concentration differences ($c_{\ell,i}^* - c_{\ell,i}$), ($c_{e,i}^* - c_{e,i}$) and ($c_{c,i}^* - c_{c,i}$) are driving forces for the diffusion and hence driving forces for crystal growth.
3. The origin of equiaxed crystals is modeled according to a continuous heterogeneous nucleation law originally developed by Oldfield [47]. This approach is based on the assumption of many potential nucleation sites in the parent melt. The nucleation sites belong to different families. Each family can only be activated as newly nucleated grains when a corresponding undercooling ΔT is achieved. The undercooling ΔT serves as the only driving force for nucleation. A Gaussian distribution is used to describe the statistical outcome of all the families of the nucleation sites.
4. No nucleation of columnar trunks is modeled. The origin of the columnar trunks is assumed to start from the mold wall, and the columnar tip front is tracked explicitly. The columnar tip front grows in the direction closest to the temperature gradient with a growth velocity, v_{tip}^c , determined by the LGK (Lipton–Glicksman–Kurz) model [2,43,48].
5. As mentioned above (Point 2), thermodynamic equilibrium solute partitioning occurs at the interface during solidification. However, for the condition of a very high cooling rate (or when the liquid diffusion coefficient of a solute element is very small), the thermodynamic equilibrium condition at the liquid/solid interface could be violated, and a solute-trapping phenomenon would occur [2,49]. The partition coefficient is no longer constant but falls in a range between the thermodynamic equilibrium partition coefficient k_i and 1, depending on the growth velocity. In the current model, the growth velocity dependent partition coefficient is not considered. Therefore, a simple approach is introduced to consider the 'solute trapping'. When the solid-side equilibrium concentration $c_{\ell,i}^*$ or $c_{c,i}^*$ becomes

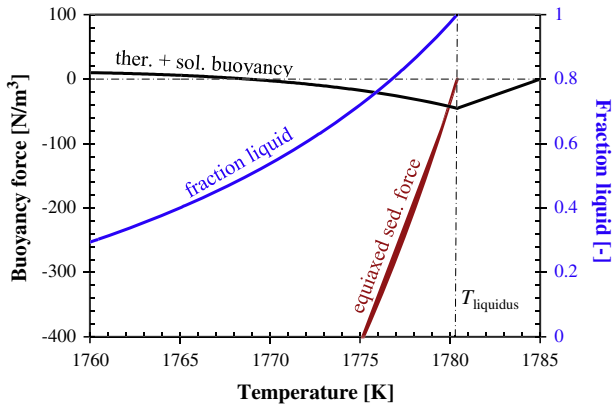


Fig. 1. Balance of different buoyancy forces as a function of temperature during solidification. As an example, here, the solidification (columnar or equiaxed) of a binary alloy (Fe–0.45 wt.%C, poured at 1785 K) is assumed, and the evolution of the solid fraction and the average liquid concentration is estimated according to the lever rule.

larger than the liquid average concentration $\bar{c}_{\ell,i}$ due to rapid cooling, we assume that the solute in the liquid with the average concentration of $\bar{c}_{\ell,i}$ is fully trapped in the solid phase. This treatment is crude but supports the general experimental fact that the segregation phenomenon disappears in a low-diffusive alloy under rapid solidification.

- The velocity fields of the melt flow and moving equiaxed crystals, \bar{u}_ℓ and \bar{u}_e , are solved. The Boussinesq approach is employed to model thermo-solutal convection and equiaxed crystal sedimentation. The densities of both the liquid and solid phases are assumed to be equal and constant; however, the thermo-solutal buoyancy forces $(f_\ell \rho_\ell^{\text{ref}} \bar{g} \sum_{i=C, Mn} [\beta_{c,i}(c^{\text{ref}} - c_{\ell,i})] + (f_\ell \rho_\ell^{\text{ref}} \bar{g} \beta_T (T^{\text{ref}} - T))$ are added in the momentum conservation equation of the melt, and the equiaxed sedimentation buoyancy force $(f_e \Delta \rho \bar{g})$ is added in the momentum conservation equation of the equiaxed phase. As an example, the different buoyancy forces as a function of T are shown in Fig. 1.

For the modeling results, the growth of columnar dendrite trunks, nucleation and growth of equiaxed crystals, thermosolutal

convection and crystal sedimentation, the columnar-to-equiaxed transition (CET) and macrosegregation are obtained. The macrosegregation is normally analyzed according to the distribution of the mixture concentration, $c_{\text{mix},i} = \sum_{j=1}^n f_j \rho_j c_{j,i} / \sum_{j=1}^n f_j \rho_j$, where j is the phase index and n is the number of phases considered. Here, we define two additional quantities: the local macrosegregation index c_i^{index} and the global macrosegregation intensity (GMI_i). The former is used to facilitate the evaluation of the positive or negative segregation according to the sign of c_i^{index} , and the latter is used to evaluate the severity of macrosegregation in the entire casting (volume average over the entire calculation domain V_{domain}).

$$c_i^{\text{index}} = \frac{c_{\text{mix},i} - c_{0,i}}{c_{0,i}} \times 100, \quad (1)$$

$$\text{GMI} = \frac{1}{V_{\text{domain}}} \cdot \iiint_{V_{\text{domain}}} |c_i^{\text{index}}| dV, \quad (2)$$

Solidification of a 2D casting ($50 \times 50 \text{ mm}^2$) of a ternary alloy (Fe–0.45 wt.%C–1.06 wt.%Mn) with three different crystal morphologies (pure columnar, pure equiaxed, or mixed columnar–equiaxed) is considered, as schematically illustrated in Fig. 2. In total, 7 cases are defined by assuming different crystal morphologies and different growth kinetics, as summarized in Table 1. The thermal boundary conditions for all the cases are identical. The casting is cooled from an initial temperature of T_0 (1777 K) in a die of T_w (373 K), and the heat transfer coefficient between the casting and the die is H_w ($300 \text{ W m}^{-2} \text{ K}^{-1}$). All the thermo-physical properties and thermodynamic data refer to the previous publication [1], as given in Table 2.

3. Columnar solidification

3.1. Solidification sequence and evolution of macrosegregation

The solidification sequences and evolution of macrosegregation ($c_{\text{max},i}^{\text{index}}$) are shown in Fig. 3. The mushy zone and f_c -isolines (volume fraction of the columnar phase) develop from the outer region toward the casting center. During solidification, a symmetric convection pattern develops; hence, only half (left) of the domain is necessarily analyzed. Initially, before solidification starts, the melt near the mold wall has a higher density due to its lower

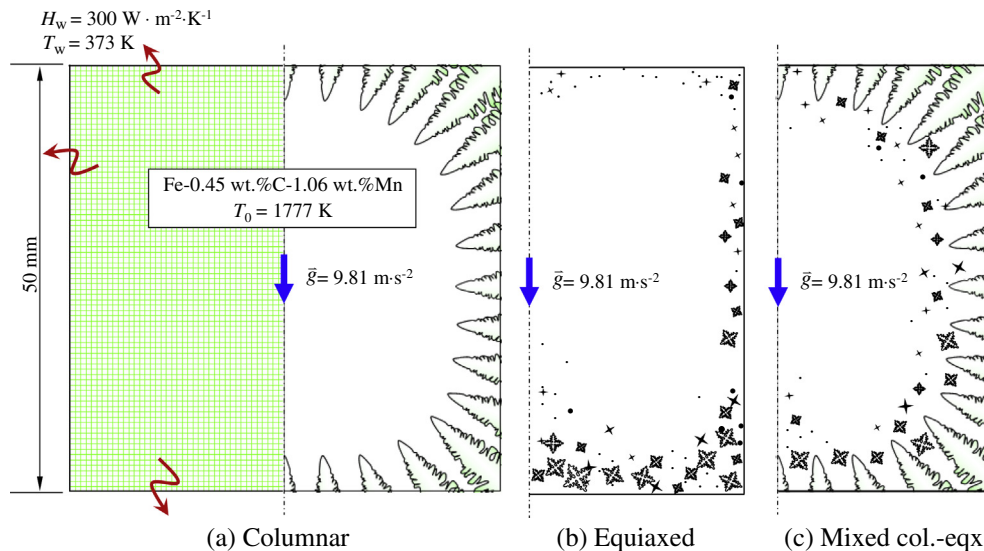


Fig. 2. A schematic of (a) pure columnar, (b) pure equiaxed and (c) mixed columnar–equiaxed solidification in a 2D ($50 \times 50 \text{ mm}^2$) domain. The thermal boundary conditions are also shown in the left half of a).

Table 1
Case definition and some of the simulation results.

	Crystal morphology	Growth kinetics ^a	$\frac{GMI_c}{GMI_{Mn}}$ ^b	c_i^{index} ^b			
				$\frac{c_{\text{min}}^{\text{index}}}{c_{\text{Mn,min}}^{\text{index}}}$	$\frac{c_{\text{max}}^{\text{index}}}{c_{\text{Mn,max}}^{\text{index}}}$	$\frac{c_{\text{min}}^{\text{index}}}{c_{\text{Mn,max}}^{\text{index}}}$	$\frac{c_{\text{max}}^{\text{index}}}{c_{\text{Mn,min}}^{\text{index}}}$
Col-I	Columnar	Diffusion-governed	$\frac{0.26}{0.076} = 3.42$	$\frac{-0.94}{-0.3}$	$\frac{0.85}{0.29}$	$\frac{1.79}{0.59}$	
Col-II	Columnar	Gulliver–Scheil	$\frac{0.19}{0.066} = 2.83$	$\frac{-0.7}{-0.25}$	$\frac{0.75}{0.27}$	$\frac{1.45}{0.52}$	
Col-III	Columnar	Lever rule	$\frac{0.39}{0.134} = 2.91$	$\frac{-0.17}{-0.61}$	$\frac{5.5}{1.95}$	$\frac{7.2}{2.56}$	
Eqx-I	Equiaxed	Diffusion-governed	$\frac{4.1}{0.34} = 12.1$	$\frac{-13.8}{-1.64}$	$\frac{43}{1.97}$	$\frac{56.8}{3.61}$	
Eqx-II	Equiaxed	Gulliver–Scheil	$\frac{10}{3.5} = 2.85$	$\frac{-23.9}{-9.0}$	$\frac{85.8}{23.1}$	$\frac{109.7}{32.1}$	
Eqx-III	Equiaxed	Lever rule	$\frac{12}{4} = 3$	$\frac{-22.8}{-8.4}$	$\frac{228}{46.4}$	$\frac{250.8}{54.8}$	
Mix-I	Mixed Col–Eqx	Diffusion-governed	$\frac{0.38}{0.11} = 3.5$	$\frac{-2.82}{-0.84}$	$\frac{1.52}{0.51}$	$\frac{4.32}{1.35}$	

^a The same model of diffusion-governed growth kinetics is used for all cases; however, very large diffusion coefficients ($10^{-6} \text{ m}^2 \text{ s}^{-1}$) of the liquid and/or solid are applied to mimic the infinite mixing of the solute for the cases using the Gulliver–Scheil and lever rule.

^b c_i^{index} (local macrosegregation index) is defined as the normalized deviation of the local mixture concentration from the nominal composition, Eq. (1), while GMI_i (global macrosegregation intensity) is defined as the volume average of the local macrosegregation index over the entire casting domain, Eq. (2).

temperature ($\beta_T = 1.43 \times 10^{-4} \text{ K}^{-1}$) and thus sinks downwards, while the hotter melt in the center rises. This process builds a large anticlockwise circulation loop. As solidification starts, the solute-enriched interdendritic melt has a lower density ($\beta_{c,c} = 1.1 \times 10^{-2} \text{ wt.\%}^{-1}$, $\beta_{c,Mn} = 2.0 \times 10^{-3} \text{ wt.\%}^{-1}$) and might rise and thus partially compensate for or reverse the above convection pattern. However, the thermal buoyancy appears to dominate over the solutal buoyancy for this initial stage. One can approximately refer to Fig. 1.

Table 2
Material properties and other parameters used for the simulations.

<i>Thermophysical properties</i>			
Specific heat	$C_{p(l)}, C_{p(s)}$	500	$\text{J kg}^{-1} \text{ K}^{-1}$
Diffusion coeff.	$D_{l,c}$	2×10^{-8}	$\text{m}^2 \text{ s}^{-1}$
	$D_{l,Mn}$	4×10^{-9}	$\text{m}^2 \text{ s}^{-1}$
	$D_{s,c}$	1×10^{-9}	$\text{m}^2 \text{ s}^{-1}$
	$D_{s,Mn}$	1.2×10^{-13}	$\text{m}^2 \text{ s}^{-1}$
Latent heat	Δh_f	2.71×10^5	J kg^{-1}
Heat conductivity	k_l, k_e, k_c	34	$\text{W m}^{-1} \text{ K}^{-1}$
Thermal exp. coeff.	β_T	1.43×10^{-4}	K^{-1}
	$\beta_{c,c}$	1.1×10^{-2}	wt.\%^{-1}
Solutal exp. coeff.	$\beta_{c,Mn}$	0.2×10^{-2}	wt.\%^{-1}
	ρ_l, ρ_e, ρ_c	6990	kg m^{-3}
Density	ρ_l, ρ_e, ρ_c	6990	kg m^{-3}
Boussinesq density diff.	$\Delta \rho$	150	kg m^{-3}
Viscosity	μ	4.2×10^{-3}	$\text{kg m}^{-1} \text{ s}^{-1}$
<i>Thermodynamic parameters</i>			
Partition coeff.	k_c	0.36	–
	k_{Mn}	0.75	–
Liquidus slope	$m_{l,c}$	–55	K (wt.\%)
	$m_{l,Mn}$	–4.8	K (wt.\%)
Eutectic temp.	T_E	1426.15	K
Melting point of Fe	T_f	1805.15	K
Gibbs–Thomson coeff.	Γ	1.9×10^{-7}	m K
Primary DAS	λ_1	5×10^{-4}	m
<i>Process parameters (I.C. and B.C.)</i>			
Initial temp.	T_0	1777	K
Heat transfer coeff.	H_w	300	K
Ambient temp.	T_w	373	K
Nucleation parameters:			
Max. equiaxed number density	n_{max}	2×10^9	m^{-3}
Undercooling for max. nucl. rate	ΔT_N	5	K
Gaussian distribution width	ΔT_σ	2	K
<i>Others</i>			
Volume element ^a	ΔV	0.65^3	mm^3
Time step ^a	Δt	0.001	s
Vol. heat transfer between phases	H^*	10^{-9}	$\text{W m}^{-3} \text{ K}^{-1}$
Packing limit	f_c^c	0.637	–
Entrapment criterion	f_e^{free}	0.2	–
CET blocking criterion	f_e^{CET}	0.49	–

^a Variation was made for study of mesh sensitivity.

The direction of the sum of the thermal and solutal buoyancy forces acts downwards initially in the vicinity of the solidification front, and this direction reverses when a certain fraction of the solid is developed and the interdendritic melt is sufficiently enriched in solutes. The reversion point of the buoyancy force direction depends on the solute enrichment of the melt and hence on the solidification diffusion kinetics. The downward flow near the columnar tip region and the upward flow in the bulk are the primary phenomena that lead to the formation of macrosegregation during the initial stage. Different segregation zones, **A** through **F**, are developed.

Afterwards, the solutal buoyancy gradually overwhelms the thermal buoyancy in the mushy region. It is clearly observed that at 40 s, the rising flow in the interdendritic mushy zone reverses the flow direction, and two circulation loops gradually develop: one clockwise in the vicinity of mushy region and one anticlockwise in the bulk region. At the late stage of solidification (60 s), only one circulation loop remains, the one driven by the solutal buoyancy. Near the casting center, only two typical segregation zones remain (the positive segregation zone **B** and the negative segregation zone **E**); the rest disappear.

The solidification ends at approximately 95 s. The final segregation patterns are shown in Fig. 4(a). As the segregation patterns of the two elements, C and Mn, are almost the same during columnar solidification, only one of these elements, i.e., C, is analyzed below. With the assumption of a stationary solid and no solidification shrinkage, the evolution of the mixture concentration in the mushy zone can be expressed as [50]:

$$\frac{\partial c_{\text{mix},i}}{\partial t} = -f_\ell \bar{u}_\ell \cdot \nabla_{\ell,i} \quad (3)$$

$$\text{i.e., } \frac{\partial c_i^{\text{index}}}{\partial t} = -\frac{100}{c_{0,i}} f_\ell \bar{u}_\ell \cdot \nabla_{\ell,i} \quad (4)$$

The evolution of $c_{\text{mix},i}$ can be analyzed from the flux of the interdendritic melt flow $f_\ell \bar{u}_\ell$ and the gradient of the liquid concentration $\nabla_{\ell,i}$. If both vectors $f_\ell \bar{u}_\ell$ and $\nabla_{\ell,i}$ point in the same direction (the angle between the two vectors is smaller than 90°), $c_{\text{mix},i}$ will decrease with time ($\partial c_{\text{mix},i}/\partial t < 0$), leading to the formation of a negative segregation. If both vectors $f_\ell \bar{u}_\ell$ and $\nabla_{\ell,i}$ point in opposite directions (the angle between the two vectors is larger than 90°), $c_{\text{mix},i}$ will increase ($\partial c_{\text{mix},i}/\partial t > 0$), leading to the formation of a positive segregation. The solute enrichment in the interdendritic mushy region is proportional to the solid volume fraction; therefore, the direction of $\nabla_{\ell,i}$ is almost perpendicular to the f_c -isolines pointing toward the casting's outer surface. At 8 s, we observe that the melt flow direction is almost but not perfectly

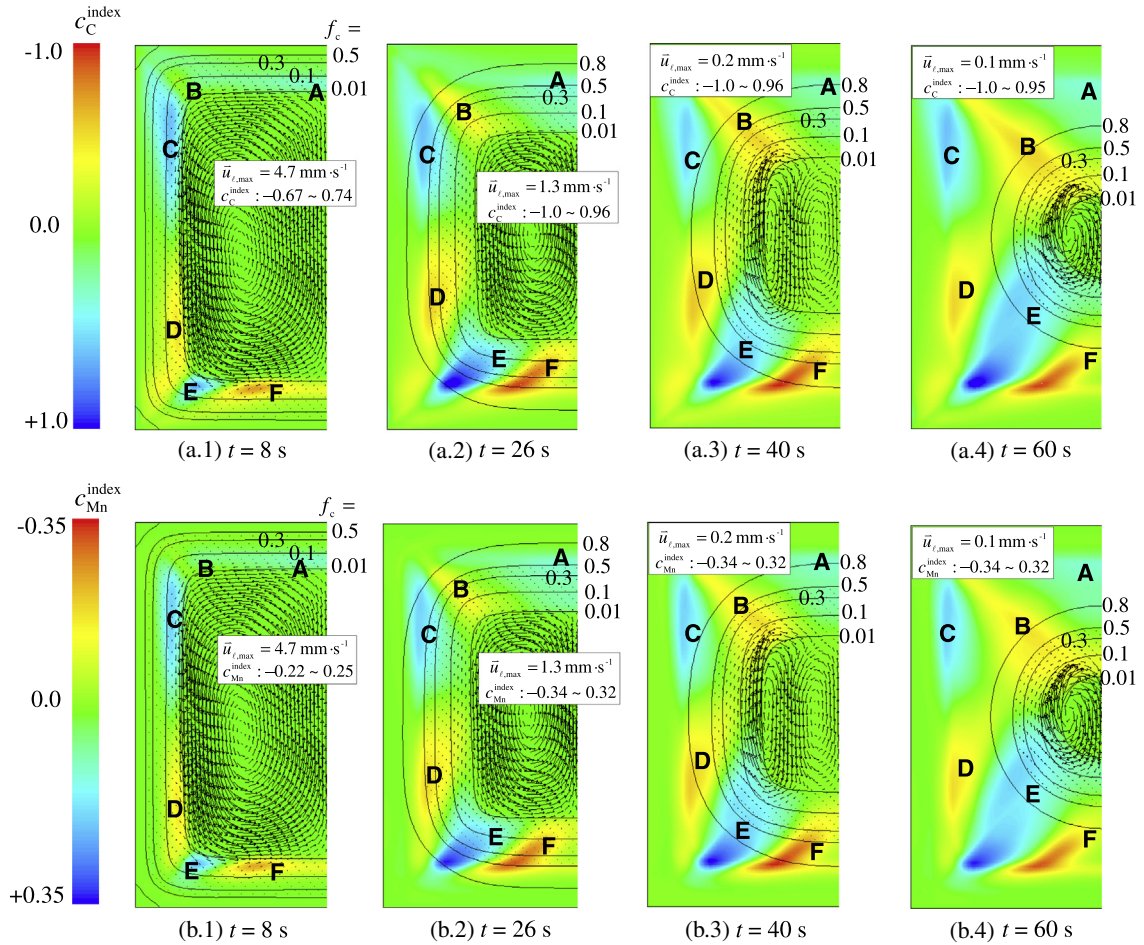


Fig. 3. Solidification sequence and evolution of macrosegregation during columnar solidification. The results for case Col-I are presented, and finite diffusion kinetics is considered. The macrosegregation indices, c_C^{index} (upper row) and $c_{\text{Mn}}^{\text{index}}$ (bottom row), are shown in the color scale, overlaid with f_c -isolines and \bar{u} vectors. The different segregation regions are marked with the symbols A–F. (For interpretation of the references to color in this figure legend, the reader is referred to the web version of this article.)

parallel to the isoline of $f_c = 0.01$. In the region where the flow direction tilts into the mushy region, a negative segregation develops, e.g., A, C and E, while in the region where the flow direction tilts away from the mushy region, a positive segregation develops, e.g., B, D and F. This mechanism applies throughout the columnar solidification process. During the late stage of solidification when the flow direction changes, the regions achieving positive or negative segregation will adapt themselves correspondingly.

3.2. Effect of diffusion kinetics

To investigate the effect of diffusion kinetics on the formation of macrosegregation, calculations of three different cases are compared, as shown in Fig. 4. Col-II and Col-III are calculated to represent the solidification processes following the lever rule and Gulliver–Scheil assumptions. The distribution range of the local macrosegregation index (from $c_{i,\text{min}}^{\text{index}}$ to $c_{i,\text{max}}^{\text{index}}$) and the global macrosegregation intensity (GMI_i) for each solute element and each case are summarized in Table 1.

- (1) The macrosegregation patterns of the 3 cases are quite different. Both the c_i^{index} distribution range ($c_{i,\text{max}}^{\text{index}} - c_{i,\text{min}}^{\text{index}}$) and GMI_i increase in the order of Col-II, Col-I, Col-III. Gulliver–Scheil underestimates GMI_C and GMI_{Mn} by 27% and 13%, respectively, while the lever rule overestimates GMI_C and GMI_{Mn} by 50% and 76%, respectively.

- (2) Meso-segregation (small channel) would be predicted by Gulliver–Scheil and lever rule kinetics, while the finite diffusion kinetics did not predict such meso-segregation. Both the Gulliver–Scheil and lever rule kinetics overestimate meso-segregation.
- (3) C is more prone to macrosegregation than Mn. GMI_C is approximately 3 times that of GMI_{Mn} . The segregation distribution patterns of both elements are very similar.

To understand the above results, detailed analysis is made: first, the effect of the diffusion kinetics on the formation of the mushy zone and microsegregation (solute enrichment in the interdendritic melt) is examined; then, the effect of the mushy zone and microsegregation on the flow pattern is examined; and finally, the effect of flow pattern on the macrosegregation is examined.

The calculations of Col-I, II and III were repeated by “switching off” the flow, and key features of the mushy zone were analyzed (Fig. 5). The major difference between Col-I and the other two cases (Col-II and III) is the mushy zone thickness. Col-I has the most extended mushy zone. For Col-I, at the lower solid fraction region, growth of the columnar trunk in the radius direction is suppressed by the finite diffusion, which leads to: (1) slowing down of the rate of latent heat release, (2) slowing down of the solute enrichment in the surrounding melt, (3) the growth of the columnar primary dendrite tip is in favor, as observed in Fig. 5(b). The temperature of the columnar primary dendrite tip is predicted to

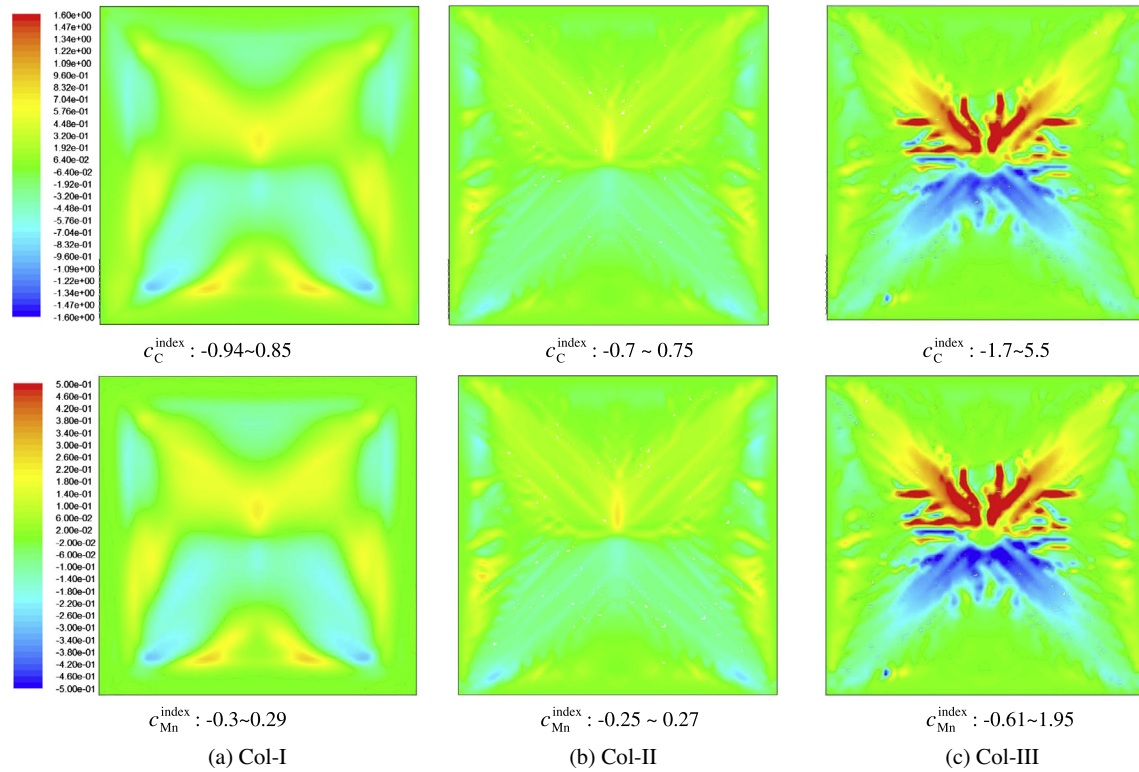


Fig. 4. Comparison of c^{index} distributions in the as-cast state assuming different growth kinetics: (a) Col-I for diffusion-governed kinetics; (b) Col-II for Gulliver–Scheil; (c) Col-III for the lever rule. The crystal morphology during solidification is purely columnar. The upper row is for C, and the bottom row is for Mn. The segregation patterns are shown as a color scale, and the segregation variation ranges are given for each figure individually. (For interpretation of the references to color in this figure legend, the reader is referred to the web version of this article.)

be approximately 1 K below the equilibrium liquidus temperature (1775.3 K for the ternary system Fe–0.45 wt.%C–1.06 wt.%Mn). In contrast, for Col-II and III, due to the assumed full mixing of the solute in the local volume element, the growth of the columnar trunk in the radius direction is overestimated, and the growth of the primary dendrite tip is underestimated. The temperature of the columnar primary dendrite tip is predicted to be 5.3 K for Col-II and 3.3 K for Col-III below the liquidus. As soon as the primary dendrite tip reaches a local volume element, a large amount of the solid will form immediately, which leads to a ‘cut’ T – f_c curve, as observed in Fig. 5(c). This type of mushy zone has a strong effect on the flow pattern and macrosegregation formation. Actually, the $(c_{\ell,c} - c_{c,c})$ curves in Fig. 5(d) do not show a large difference between the three cases.

One may argue that tracking of the columnar primary dendrite tip is not necessary with a model considering the infinite diffusion kinetics (Col-II or III). Then, there would be no ‘cut’ T – f_c curve (Fig. 6), and a similar extended mushy zone to the case Col-I would be predicted. However, this type of model is not useful for mixed columnar–equiaxed solidification. A necessary feature of the mixed columnar–equiaxed solidification model is to track the columnar primary dendrite tip front to consider the competition between growths of columnar and equiaxed phases.

The effect of the mushy zone and microsegregation on the flow pattern and subsequently on the macrosegregation is analyzed in Fig. 7. A comparison of the flow patterns (at the moment when 50% of the casting is solidified) of the three cases is made. The interdendritic flow can only be observed in the mushy region where the solid fraction is less than 30%. The flow in the extended mushy zone of Col-I is relatively easier. The interdendritic melt (solutal buoyancy dominant) is lighter and tends to rise, while in

front of the columnar tips, the flow (thermal buoyancy dominant) remains downward. The flow direction near the columnar primary dendrite tip front reverses. For Col-II and Col-III, the predicted mushy region with a solid fraction of less than 30% is very narrow; therefore, the interdendritic flow is confined in the narrow region, and no upward flow in the mush is observed at this moment. The magnitudes of the flow of the three cases are also quite different. Note that the flow patterns change transiently, and even the flow direction in the casting center reverses at the late stage of solidification.

The effect of the flow on the macrosegregation formation is described by Eq. (4). As demonstrated in the upper row of Fig. 7, the evolution of macrosegregation, being quantified by $\partial c_{\text{mix},c} / \partial t$, depends on the flow direction \vec{u}_i in black vector) and the direction of the liquid concentration gradient ($\nabla c_{\ell,c}$ in red vector). The two vectors pointing in the same direction (angle less than 90°) lead to a reduction of $c_{\text{mix},c}$, i.e., the formation of negative segregation; conversely, the two vectors pointing in opposite directions lead to an increase of $c_{\text{mix},c}$, i.e., the formation of positive segregation.

We predict that the global macrosegregation intensity increases in the order of Col-II, Col-I, Col-III. The reason is as follows. As an example, the result at the moment when 50% of the casting is solidified, Fig. 7, shows that the positive and negative extremes of $\partial c_{\text{mix},c} / \partial t$ increase in the order of Col-I, Col-II, Col-III. This result helps to explain why the most severe segregation occurs for Col-III. However, we also see that the area to develop the macrosegregation for Col-I is much broader than those for the other two cases, as observed in the upper row of Fig. 7. This finding explains why Col-I has more intensive segregation than Col-II. Another feature is that the area with non-zero of $\partial c_{\text{mix},c} / \partial t$ is mainly distributed in the front of the mushy zone with a solid fraction less than 0.3.

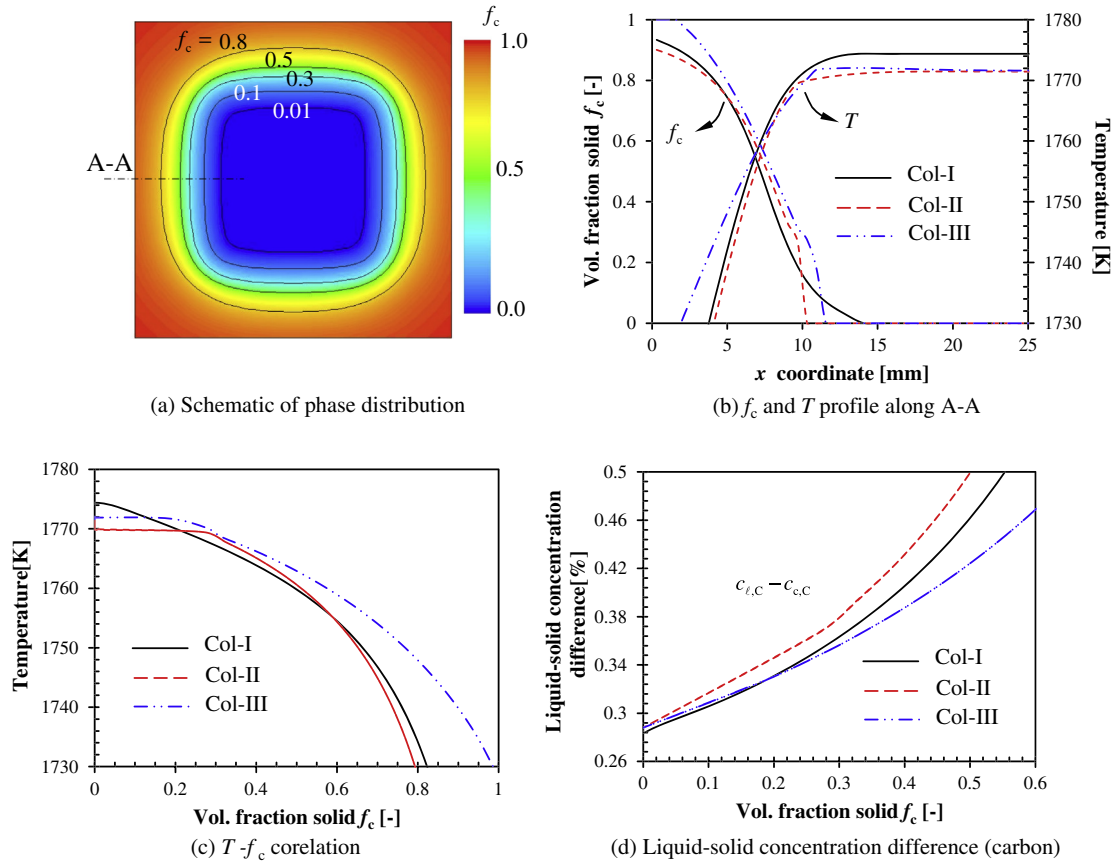


Fig. 5. Effect of growth kinetics on the formation of mushy zone during pure columnar solidification. The calculations of Col-I, II and III are repeated by “switching off” the flow; however, the columnar primary dendrite tip front is tracked using the LGK model [2,43,48]. The results are evaluated along a path A–A at the moment when 50% of the entire casting domain is solidified: (a) global f_c distribution (Col-I); (b) f_c and T profiles along the path A–A; (c) T - f_c curves; and (d) liquid–solid concentration difference ($c_{l,c} - c_{c,c}$) as a function of f_c .

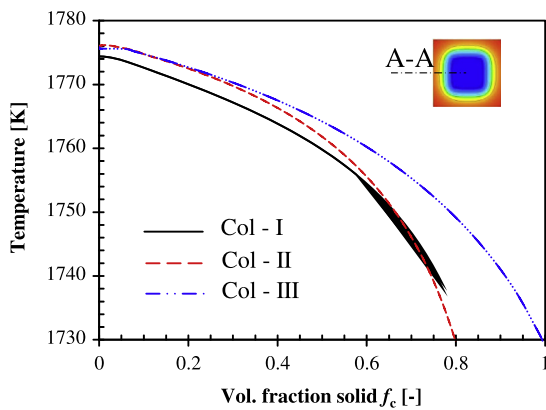


Fig. 6. T - f_c curves of Col-II and Col-III without tracking the columnar primary dendrite tip. The columnar primary dendrite tip front is set to be the liquidus isotherm.

This area is very narrow for Col-II and Col-III, and the flow is relatively unstable. The instability of flow in the front of the mushy zone is the origin of meso-segregation.

4. Equiaxed solidification

4.1. Solidification sequence and evolution of macrosegregation

The solidification sequence and formation of macrosegregation are shown in Fig. 8. Although the thermo-solutal convection and

crystal sedimentation are coupled, the crystal sedimentation and induced flow dominate. As soon as the equiaxed phase appears, the equiaxed sedimentation force dominates over other thermo-solutal buoyancy $\Delta\rho = 150 \text{ kg m}^{-3}$, the solid phase is heavier than the melt), as illustrated in Fig. 1. The flow and crystal sedimentation are unsymmetrical and unstable. The start of cooling at the casting corner and surface stimulates the immediate nucleation and growth of equiaxed crystals. The equiaxed grains sink downwards (Fig. 8(a.1) and (b.1)), dragging down the surrounding melt. Thus, the melt in the bottom region moves inwards and then rises up in the middle, providing space for the oncoming grains and melt. Hence, two vortices form in the bulk. In turn, the melt flow affects the motion of the crystals. The motion of the crystals increases the fraction of solid f_c in the base region and causes f_c to increase and extend the packing limit (0.637) near $t = 16 \text{ s}$ (Fig. 8(b.3)) such that the motion of the crystals ceases. This phenomenon is known as grain settlement or sedimentation. Grain sedimentation affects the solid phase distribution. The f_c isolines in the lower part evidently proceed much faster than those in the upper part, and notably, the f_c isolines even protrude upwards into the casting center. The upward melt flow at the casting center tries to bring crystals upwards due to a drag force, while the crystals themselves attempt to keep sinking downwards due to gravity. Another effect of the melt flow on the motion of crystals can be observed in the upper part of the casting, where the crystals near the upper boundary do not sink directly. Instead, the crystals first move toward (or diverge to) the upper corners (Fig. 8(b.1)–(b.4)), then follow the main stream of the flow along the side walls, and, finally, settle in the bottom region.

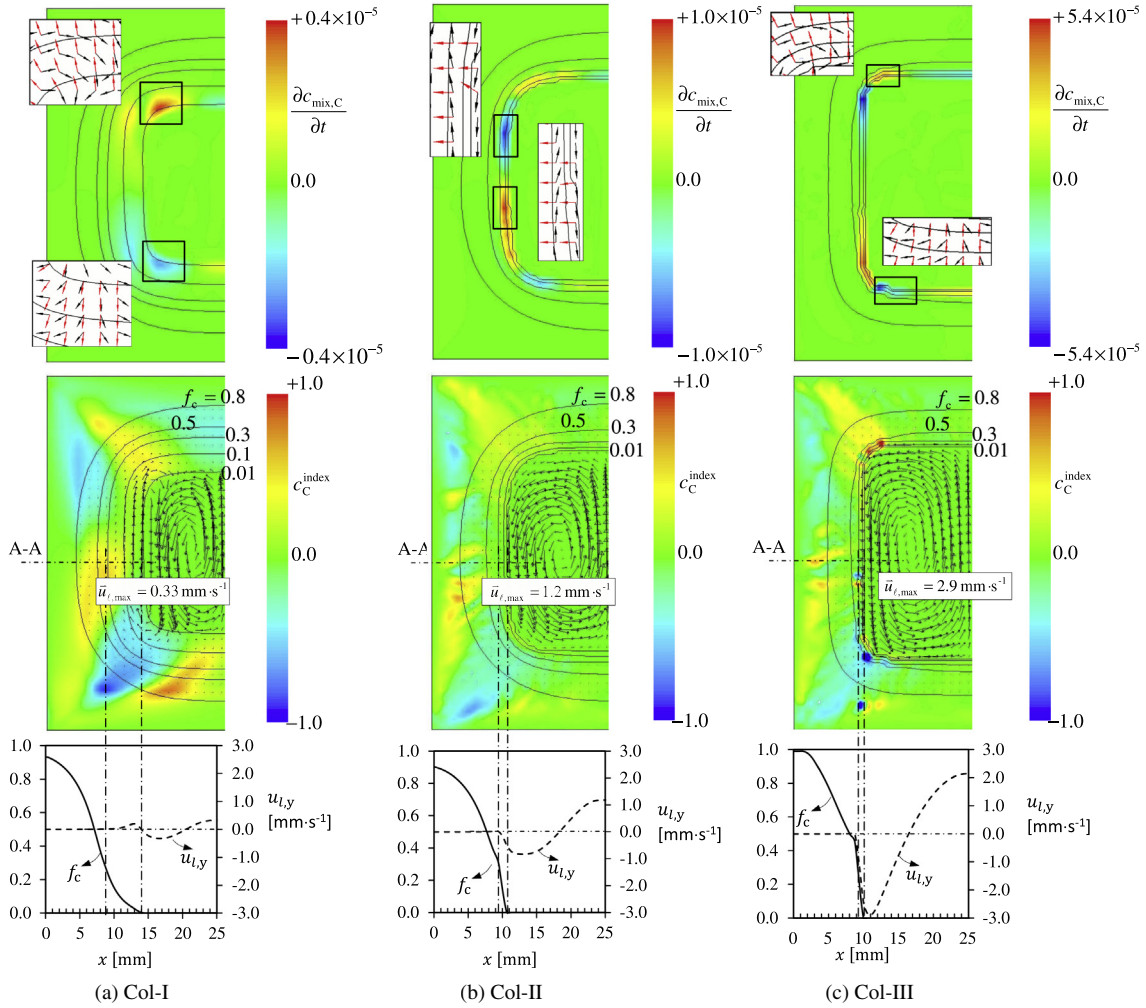


Fig. 7. Analysis of the macrosegregation formation during pure columnar solidification. Three growth kinetics are compared: (a) Col-I, (b) Col-II and (c) Col-III. The results are evaluated at the moment when 50% of the entire casting domain is solidified. Upper row: calculated distribution of $\partial c_{\text{mix},C}/\partial t$, and the vector directions of \vec{u}_l (in black) and $\nabla c_{l,C}$ (in red) are shown in some marked regions. Middle row: distribution of c_C^{index} and liquid velocity field. The fraction of solid (columnar) isolines are also shown. Low row: distribution of f_c and y-component of liquid velocity along the path A-A. (For interpretation of the references to color in this figure legend, the reader is referred to the web version of this article.)

In Fig. 8, different segregation zones are marked by the symbols **A** through **E**. During equiaxed solidification, different segregation zones develop and disappear dynamically. The final segregation pattern is shown in Fig. 9(a).

With the dominance of crystal sedimentation in the macroscopic transport phenomena, the evolution of different segregation zones during equiaxed solidification can be analyzed by [50,51]:

$$\frac{\partial c_{\text{mix},i}}{\partial t} \approx (c_{\ell,i} - c_{e,i}) \nabla \cdot (f_e \vec{u}_e). \quad (5)$$

$$\text{or } \frac{\partial c_i^{\text{index}}}{\partial t} \approx \frac{100}{c_{0,i}} (c_{\ell,i} - c_{e,i}) \nabla \cdot (f_e \vec{u}_e). \quad (6)$$

The positive segregation **A** and negative segregation **B** begin from the lower bottom region. These segregations are caused by a separation of the solute-enriched melt ($c_{\ell,i} > c_{0,i}$), i.e., ($c_{\ell,i} > c_{e,i} > 0$). Near the vertical center line, the melt rises, while the crystals tend to sink and settle (pile up) at the bottom. In the lower bottom region **B**, the equiaxed phase accumulates, i.e., $\nabla \cdot (f_e \vec{u}_e) \leq 0$, leading to the formation of negative segregation. In region **A**, $\nabla \cdot (f_e \vec{u}_e) \geq 0$, positive segregation occurs. The positive segregation region **A** is not stationary but moves

upwards with the flow. The negative segregation region **B** stays at the bottom, becoming gradually extended, and thus, the segregation intensifies as the sedimentation process continues. The negative segregation regions **C** form by the same mechanism as region **B**; however, these regions are mostly located in the bulk region, where the volume fraction of the equiaxed phase remains smaller than the packing limit (0.637). These regions are not stationary and move with the flow. The positive segregation region **D** on the upper surface is caused by crystals leaving this zone. The solute-depleted crystals leave the region **D**, while the solute-enriched melt is left behind, resulting in the positive segregation of region **D**. The crystals leaving region **D** form a negative segregation zone **E** just below. The formation of the positive segregation region **D** and the negative segregation zone **E** can also be explained by Eq. (6). The motion of the crystals in region **E** is strongly affected by the global flow pattern. With time, this region will merge with region **C**, follow the flow stream and form the final segregation pattern, as shown in Fig. 9(a). The unsymmetrical distribution of macrosegregation is caused by the flow instability.

An interesting finding is that the two elements C and Mn behave differently in the formation of segregation, differing not only in intensity but also in the distribution pattern. In Fig. 8(c.1), the positive segregation region **D** near the top surface

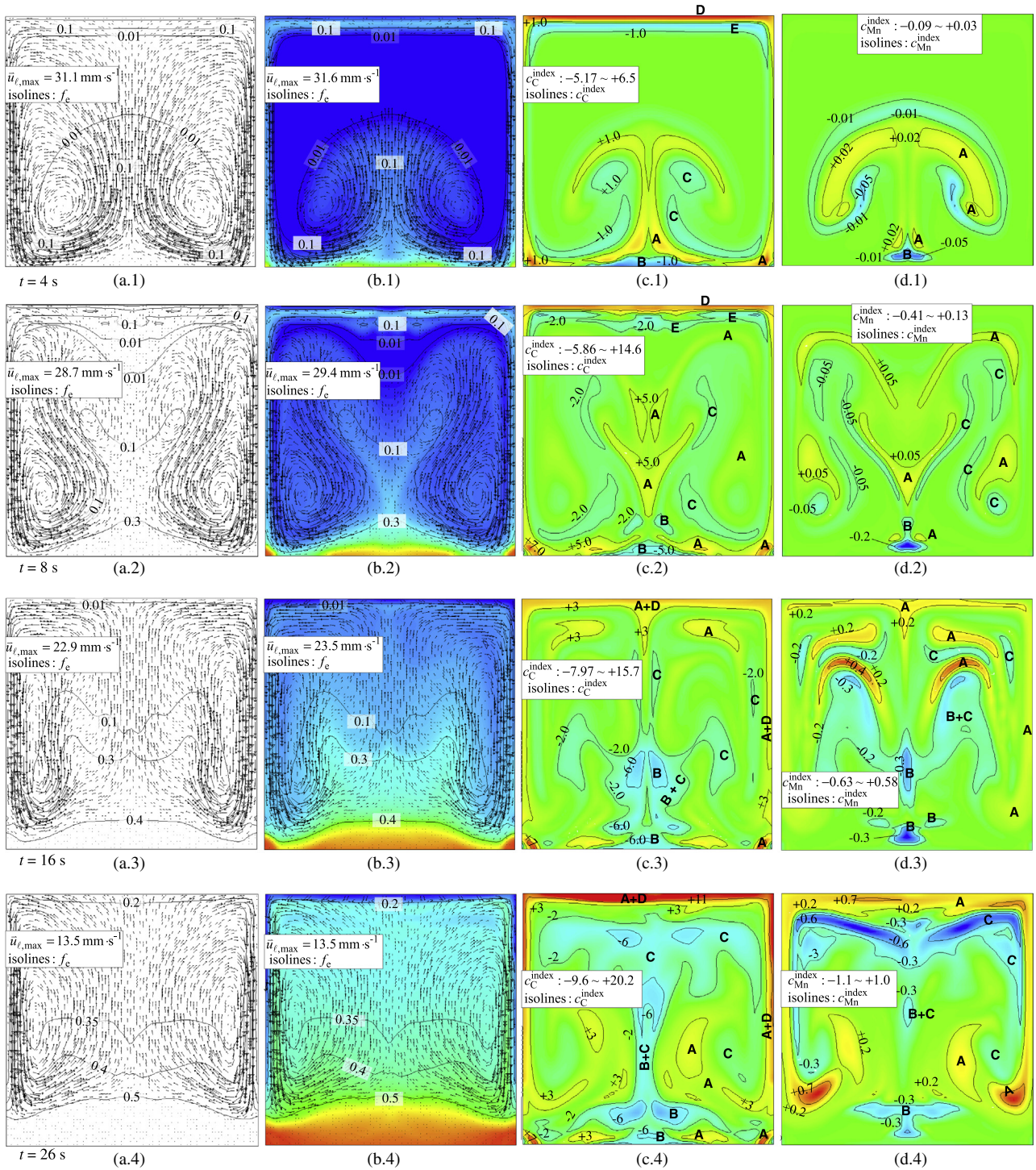


Fig. 8. Solidification sequence and evolution of macrosegregation during equiaxed solidification. The results for the case Eqx-I are presented, and finite diffusion kinetics is considered. \bar{u}_t and \bar{u}_e are shown in vectors, (a) and (b), overlaid with f_e -isolines. The macrosegregation indices, c_C^{index} (c) and $c_{\text{Mn}}^{\text{index}}$ (d), are shown in the isolines. The different segregation regions are marked with the symbols A–E. f_e , c_C^{index} and $c_{\text{Mn}}^{\text{index}}$ are also shown in the color scales in addition to the isolines, with blue for the minimum (or negative extreme), green for the middle value and red for the maximum. (For interpretation of the references to color in this figure legend, the reader is referred to the web version of this article.)

and the negative segregation region E just below are visible for the alloy element C; however, these regions cannot be observed for the element Mn (Fig. 8(d.1)). We have analyzed the solidification path of this casting in Part 1 (Section 3). Due to the large difference between the two alloy elements (C and Mn) in terms of the diffusion coefficients ($D_{\text{C}} = 2 \times 10^{-8}$, $D_{\text{Mn}} = 4 \times 10^{-9} \text{ m}^2 \text{ s}^{-1}$) and solute partition coefficients ($k_{\text{C}} = 0.36$, $k_{\text{Mn}} = 0.75$), the rate of solute

enrichment of C in the melt is much higher than that of Mn. At the very initial stage, the cooling rate near the casting surface is so high that ‘solute trapping’ occurs for the element Mn. Therefore, no segregation of Mn in that region at the initial stage can be observed.

The final segregation patterns of both elements exhibit some similarities; however, the difference in the intensity is large

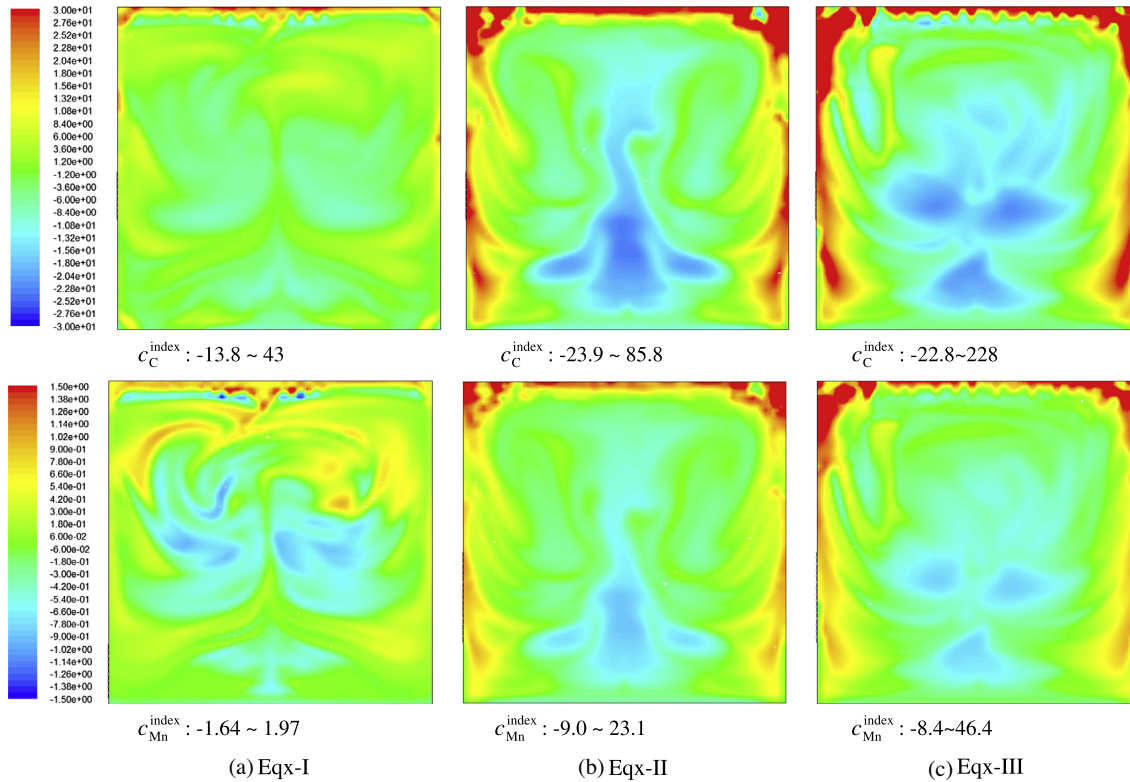


Fig. 9. Comparison of c_i^{index} distributions in the as-cast state by assuming different growth kinetics: (a) Eqx-I for diffusion-governed kinetics; (b) Eqx-II for Gulliver–Scheil; and (c) Eqx-III for the lever rule. The crystal morphology during solidification is purely equiaxed. The upper row is for C, and the bottom row is for Mn. The segregation patterns are shown in the color scale, and the segregation variation ranges are given for each figure individually. (For interpretation of the references to colour in this figure legend, the reader is referred to the web version of this article.)

(Fig. 9(a)): the C segregation index falls in the range of -13.8 to 43% , while the Mn segregation index is in the range of -1.64 to 1.97% . The segregation range of C in the as-cast state is 15.7 times larger than that of Mn.

4.2. Effect of diffusion kinetics

To investigate the effect of diffusion kinetics on the formation of macrosegregation, calculations of three different cases are compared, as shown in Fig. 9. Eqx-II and Eqx-III are calculated to represent the solidification processes following the lever rule and Gulliver–Scheil assumptions. The distribution range of the local macrosegregation index (from $c_{i,\text{min}}^{\text{index}}$ to $c_{i,\text{max}}^{\text{index}}$) and the global macrosegregation intensity (GMI_i) for each element and each case are summarized in Table 1.

- (1) As the global flow/sedimentation patterns of cases Eqx-II and Eqx-III are quite similar to that of Eqx-I, the macrosegregation patterns of the 3 cases exhibit some similarities. However, large differences in segregation intensity were observed. Both the (c_i^{index} distribution range $c_{i,\text{max}}^{\text{index}} - c_{i,\text{min}}^{\text{index}}$) and GMI_i increase significantly in the order of Eqx-I, Eqx-II, Eqx-III. Calculations based on Gulliver–Scheil or the lever rule dramatically overestimate macrosegregation. Gulliver–Scheil overestimates GMI_C and GMI_{Mn} by 1.44 and 9.3 times, respectively, while the lever rule overestimates GMI_C and GMI_{Mn} by 1.92 and 10.7 times, respectively.
- (2) C is more prone to macrosegregation than Mn. GMI_C is approximately 3 times that of GMI_{Mn} for Eqx-II and Eqx-III, while GMI_C is approximately 12 times that of GMI_{Mn} for Eqx-I.

Similar analysis as in Section 3.2 was performed. Additional calculations for Eqx-I, II and III were performed by “switching off” the flow. The key features of the two-phase region are shown in Fig. 10. In the low fraction solid region, all three cases show similar phase distributions (Fig. 10(b)); Eqx-I solidifies at a relatively lower temperature (Fig. 10(c)); and the ($c_{i,C} - c_{e,C}$) of Eqx-I is predicted to be slightly smaller (Fig. 10(d)) than the other two cases. In the high fraction solid region, the phase distribution of Eqx-I is quite similar to that of Eqx-II but quite different from that of Eqx-III (Fig. 10(b)); the curves of ($c_{i,C} - c_{e,C}$) among the three cases are different from each other.

It remains difficult, only based on the result of Fig. 10, to explain the observed difference in macrosegregation among the three cases (Fig. 9) when flow and crystal sedimentation are considered. The solidification behavior in the high fraction solid region plays an ignorable role in the formation of macrosegregation, although some large difference in the solid fraction between Eqx-III and the other two cases is observed because flow/sedimentation would stop in this region. The minor difference in ($c_{i,C} - c_{e,C}$) among the three cases in the low fraction solid region would to some extent affect the calculation of macrosegregation but appears insufficient to explain the observed difference in macrosegregation of Fig. 9. Therefore, further analysis based on the flow/sedimentation is performed below.

Detailed analysis of the distributions of $(c_{i,C} - c_{e,C}) \nabla \cdot (f_e \bar{u}_e)$ and $\partial c_{\text{mix},C} / \partial t$ is shown in Fig. 11. For all three cases, $\partial c_{\text{mix},C} / \partial t$ exhibits almost the same distribution pattern as $\nabla \cdot (f_e \bar{u}_e)$. This finding hints that flow/sedimentation plays a more important role in the formation of macrosegregation. The sign of $\nabla \cdot (f_e \bar{u}_e)$ is an indicator for the local solid phase accumulation/depletion by transport of equiaxed crystals. The extreme values (the distribution range given

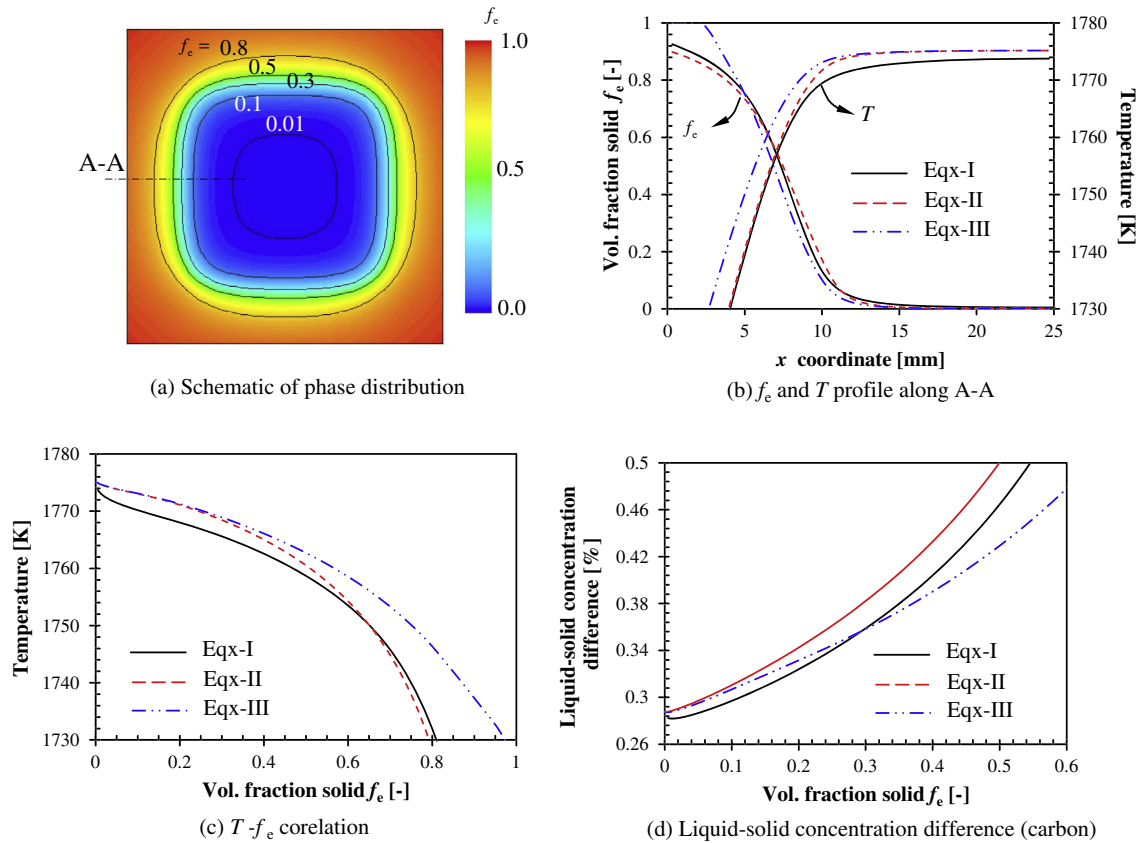


Fig. 10. Effect of growth kinetics on the two-phase region during pure equiaxed solidification. The calculations of Eqx-I, II and III are repeated by “switching off” the flow. The results are evaluated at the moment when 50% of the entire casting domain is solidified. (a) f_e distribution for Eqx-I. (b) f_e and T profiles along the path A–A as marked in a. (c) T – f_e curves. (d) Carbon concentration difference between the inter-granular melt and equiaxed phase ($c_{l,c} - c_{e,c}$) as a function of f_e .

in the figures) of $\partial c_{\text{mix},c}/\partial t$ indicate that the evolution rate of macrosegregation increases in the order of Eqx-I, Eqx-II and Eqx-III.

One may argue that Fig. 11 only shows the result at the moment when 25% of the casting domain is solidified and that it is not sufficient to explain the final macrosegregation, which is the result of dynamics of the entire solidification and sedimentation processes. Therefore, a statistical study on the history of GMI_C and the domain-averaged quantities ($c_{l,c} - c_{e,c}$) and $|\partial c_{\text{mix},c}/\partial t|$ was performed, and the results are plotted against the domain-averaged solid fraction (Fig. 12). The change of GMI_C during solidification follows the trend of $|\partial c_{\text{mix},c}/\partial t|$. Both GMI_C and the domain-averaged $|\partial c_{\text{mix},c}/\partial t|$ of Eqx-I are smaller than those of the other two cases. This finding means that a case considering finite diffusion kinetics is less prone to macrosegregation. Comparing Eqx-II and Eqx-III, we observe that GMI_C and the domain-averaged $|\partial c_{\text{mix},c}/\partial t|$ cross each other at the moment when the casting is approximately 30% solidified. More severe segregation is predicted for Eqx-III (lever rule) than for Eqx-II (Gulliver–Scheil), although the domain-averaged ($c_{l,c} - c_{e,c}$) curve of Eqx-II is always higher than that of Eqx-III. This result is due to the dominant contribution of $\nabla \cdot (f_e u_e)$. With the current benchmark configuration, the sedimentation phenomenon of Eqx-III is predicted to be more severe than the other two cases at the late stage of solidification.

5. Mixed columnar–equiaxed solidification

The modeling result indicates that the selected Fe–C–Mn alloy tends to solidify in a dominantly columnar or mixed columnar–equiaxed structure in the current benchmark of small dimension. The appearance of a columnar structure has a strong

effect (resistance) on the flow and, hence, on the formation of macrosegregation. The solidification sequence and the formation of macrosegregation are shown in Fig. 13. Both the columnar and equiaxed phases grow and compete with each other. The equiaxed grains sink from the top surface and along the two side walls, while the columnar phase develops almost equally from all four walls. The melt is dragged downwards by the sinking equiaxed grains, which further induces an upward flow of the melt in the middle of the casting. Two symmetrical convection rolls form. The contribution of thermal and solute buoyancy to the global flow is relatively small. The casting condition favors the growth of the columnar structure. As no sufficient equiaxed phase appears ahead of the columnar front to block the growth of the primary dendrite tips of the columnar trunks, the columnar tip fronts finally meet in the casting center. No columnar-to-equiaxed transition (CET) is predicted. The final as-cast structure contains a dominant columnar phase with only 2–15% of the equiaxed phase being captured by the columnar trunks.

If we compare the case of mixed columnar–equiaxed solidification (Mix-I) with that of pure equiaxed solidification (Eqx-I), the appearance of a columnar structure reduces the liquid and equiaxed velocities by one order of magnitude. If we compare the case of Mix-I with that of Col-I, the melt flow of Mix-I is stronger than that of Col-I; however, their velocities are of the same magnitude. The macrosegregation in the case Mix-I is predicted to be much less severe than that of Eqx-I but is of course stronger than that of Col-I. The difference among the cases Col-I, Eqx-I and Mix-I can be observed not only by the severity but also by the distribution pattern. The evolution of the different segregation zones, A through E, for the case of Mix-I is also shown in Fig. 13(c).

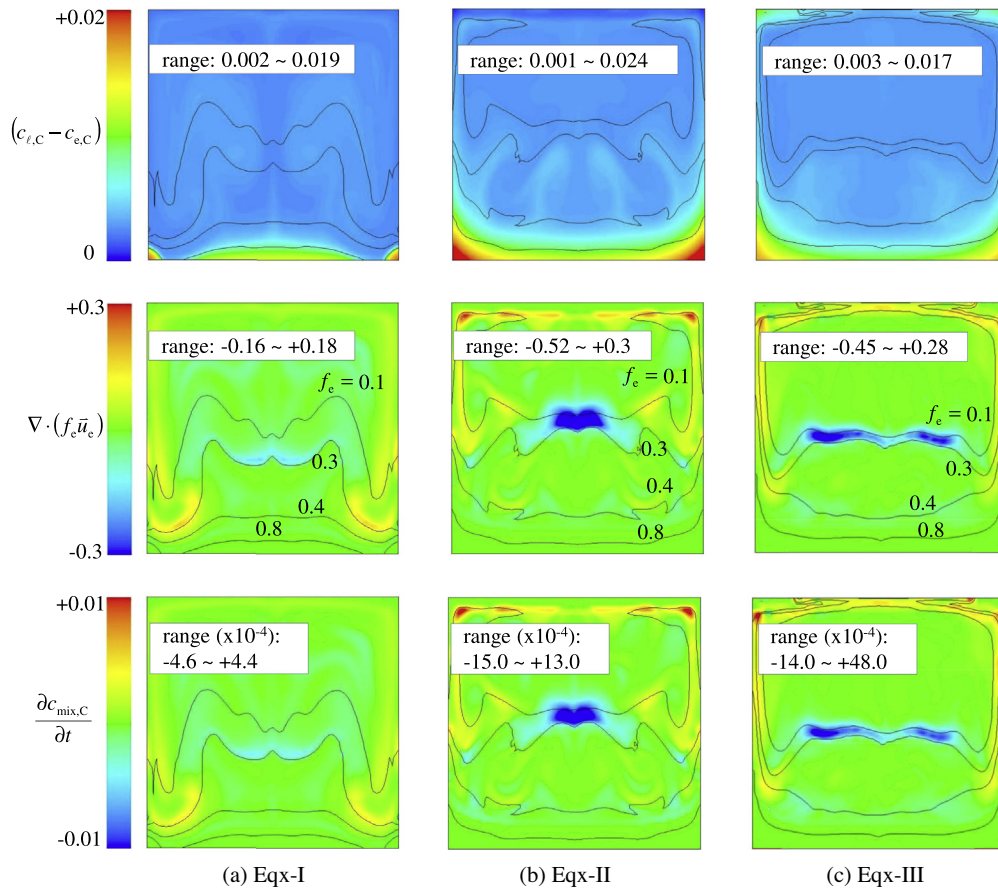


Fig. 11. Analysis of the macrosegregation formation during pure equiaxed solidification by different growth kinetics: (a) Eqx-I, (b) Eqx-II and (c) Eqx-III. The results are evaluated at the moment when 25% of the entire casting domain is solidified. Upper row: distribution of liquid–solid carbon concentration difference ($c_{l,C} - c_{e,C}$). Middle row: distribution of $\nabla \cdot (f_e \bar{u}_e)$. Low row: the distribution of $\partial c_{\text{mix},C} / \partial t$. f_e -isolines are also shown.

A detailed analysis of the macrosegregation mechanisms for mixed columnar–equiaxed solidification is beyond the scope of the current paper. Readers can refer to previous publications of the authors [43,44,50].

6. Solidification of an industry ingot

Segregation in a 2.45-ton ingot was reported in [52]. The nominal composition¹ of the ingot was Fe–0.41 wt.% C–1.06 wt.%Mn–0.48 wt.%Si–0.056 wt.%S–0.052 wt.%P. Here, only a ternary system, namely two alloy elements (C and Mn), is considered. The sulfur print and the measured segregation of C and Mn are shown in Fig. 14(a)–(c). The segregation maps are reproduced by interpolation of the original chemical analyses of 53 drilling samples out of the ingot section. The segregation maps of both elements, C and Mn, look similar in most parts of the section but differ in the hot top region. An overall negative segregation (except for two points) along the centerline is observed, while in the hot top region, a large positive segregation of C is observed. The sulfur print (Fig. 14(a)) shows a discontinuous segregation pattern (broken lines) in the middle radius region between the outer surface and the central axis of the ingot. This zone corresponds to a slightly positive segregation, as becomes evident from the segregation maps (Fig. 14(b) and (c)). Configuration of this ingot for the simulation together with necessary boundary

and initial conditions are described in Fig. 14(d). More details about the process parameters can be found elsewhere [53,54]. The ingot had a square cross-section and was cast in a chilled mold; however, a 2D-axis symmetrical simulation was performed to approximate the solidification behavior in the square section ingot. The predicted solidification sequence is shown in Fig. 15, and the segregation map is shown in Fig. 16(a) and (b). The same material data as the previous benchmark (Table 2) are used.

First, the flow during solidification is unstable (Fig. 15). The melt flow in the bulk region ahead of the columnar dendrite tip front is driven by three mechanisms: (i) solutal buoyancy driving upwards, (ii) thermal buoyancy driving downwards, and (iii) equiaxed sedimentation, which drags the surrounding melt downwards. The two downward driving forces dominate, and the melt flows downwards along the columnar dendrite tip front. This downward flow along the columnar tips forces the melt to rise in the ingot center. This rising melt interacts with the falling equiaxed crystals and with the downward flow near the columnar tip front to form many local convection cells. These convection cells are developed or suppressed dynamically; thus, the flow direction in the cells changes with time. The sinking of the equiaxed crystals in front of the columnar dendrite tips leads to an accumulation of the equiaxed phase in the base region of the ingot. These accumulated equiaxed crystals in the base region block the growth of the columnar dendrite tips, i.e., CET occurs, finally causing the formation of a characteristic cone-shaped distribution of the equiaxed zone. Correspondingly, relatively strong negative segregation for both elements C and Mn is predicted in the low-bottom equiaxed zone (Fig. 16(a) and (b)). With the sedimentation of a large number

¹ The nominal carbon concentration is 0.41 wt.%; however, the post-mortem chemical analyses of the drilling samples indicate an averaged carbon concentration over the whole ingot of 0.45 wt.%. Therefore, the simulation is performed with an initial carbon concentration of 0.45 wt.%.

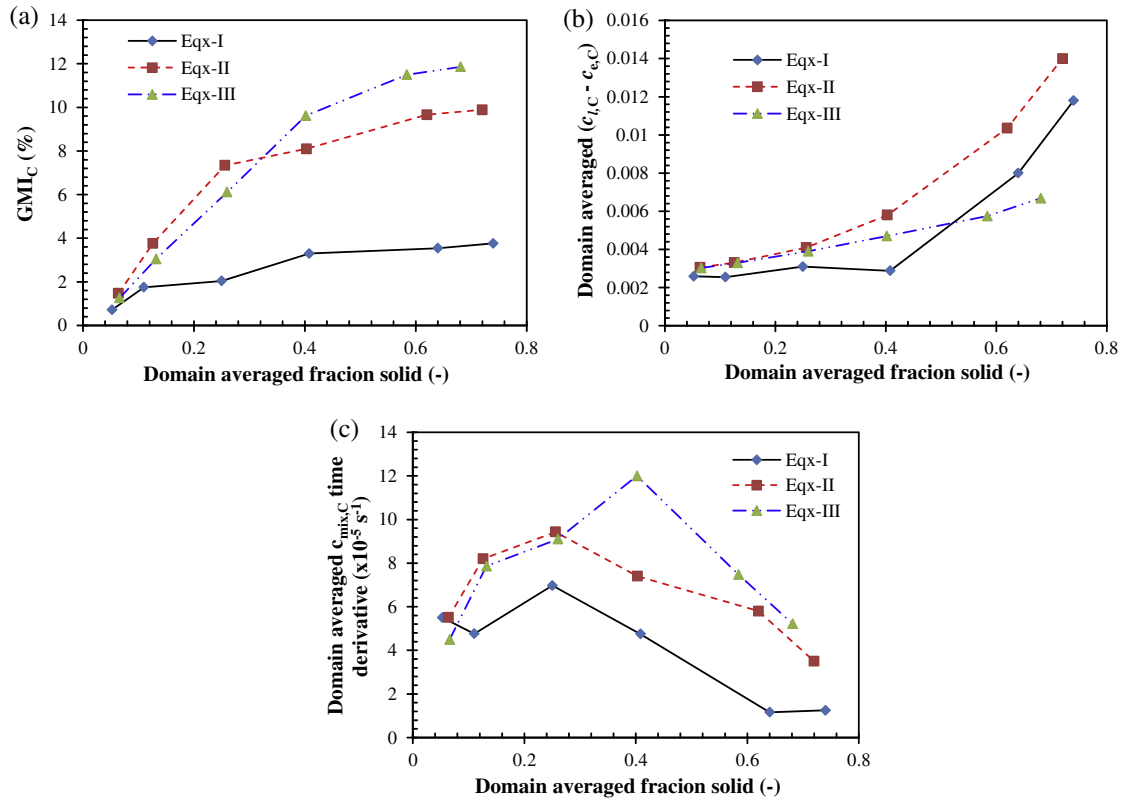


Fig. 12. Evolution of global macrosegregation during equiaxed solidification as a function of the domain-averaged fraction solid ($\sum f_e \Delta V_i / \sum \Delta V_i$), where ΔV_i is the volume of each volume element. (a) GMI_C; (b) $\sum (c_{i,C} - c_{e,C}) \Delta V_i / \sum \Delta V_i$; (c) $\sum (\partial c_{mix,C} / \partial t) \Delta V_i / \sum \Delta V_i$.

of equiaxed crystals, the solute-enriched melt is pushed upwards in the casting center, causing a positive segregation in the upper region.

Second, a streak-like segregation (Fig. 16(a) and (b)) in the middle radius zone between the outer surface and the central axis of the ingot is predicted. The following tentative hypothesis concerning this streak-like segregation is proposed: as the equiaxed crystals can be captured (crystal entrapment) by the growing columnar trunks, the entrapment of the equiaxed crystals will lead to a heterogeneous phase distribution between the columnar and equiaxed crystals behind the columnar tip front, which can be observed in Fig. 15(b)–(d). The resistance to the interdendritic flow by the columnar trunks and the entrapped equiaxed crystals is different. Therefore, the flow direction of the melt in this region is slightly diverted by the heterogeneous phase distribution. As the formation of macrosegregation is extremely sensitive to the interdendritic flow, it is not surprising that the induced macrosegregation (Fig. 16(a) and (b)) assumes the similar streak-like pattern of the phase distribution (Fig. 15(d)).

One may notice that the predicted streak-like segregation zone appears to coincide with the discontinuous segregation (broken lines) zone in the middle radius zone between the outer surface and the central axis of the ingot, as indicated by the sulfur print (Fig. 14(a)). This discontinuous segregation is suspected to be the channel segregation, namely, an A-segregation (or A-segregates). However, based on the current numerical simulation, it remains unclear whether the classical A-segregation is the same as or originates from the streak-like segregation. According to the most widely accepted empirical explanation, an A-segregation originates and develops in the columnar dendritic mushy zone and is accompanied by remelting. A recent study by the authors [55,56] in a Sn–Pb laboratory casting has shown that channel segregation can originate and develop during pure columnar solidification, where no equiaxed crystals exist. Therefore, we have named the streak-like

segregation here a quasi-A-segregation. To form this quasi-A-segregation, the sedimentation of equiaxed crystals and its interaction with the columnar tip front and melt flow appear to play an important part. More details about the formation mechanism for this type of quasi-A-segregation can be found elsewhere [54].

The predicted segregation along the ingot centerline is compared with the experimental result in Fig. 16(c) and (d). Some agreements are achieved; however, the quantitative discrepancy remains significant. Both simulations and experiments show a negative segregation along the centerline in the lower and middle parts for both elements C and Mn. The predicted negative segregation in the base region is much stronger than the experimental one for both elements C and Mn, which means that the simulation overestimates the negative segregation in the base region. This negative segregation is caused by the crystal sedimentation. In the hot top region, both experiments and simulations show positive segregation of C; however, the positions are different. The simulation predicts a positive segregation of Mn in the hot top region, while the experiment shows only two points with slightly positive segregation in the upper part of the centerline, and thus, the predicted and experimentally observed positions of the positive segregation are not in agreement.

The quantitative discrepancy above arises due to the following two factors. One factor is the model assumptions. As observed in [53,54], the assumption of globular equiaxed morphology can overestimate the sedimentation-induced negative segregation. Conventional steel would mostly solidify with dendritic morphology. In addition, the uncertainty about the nucleation parameters for the origin of equiaxed crystals might also cause errors in the calculation of macrosegregation. Moreover, the solidification shrinkage, mechanical deformation and turbulence of the flow are not treated. The second factor concerns the assumed process parameters and mainly the thermal boundary conditions. The heat transfer coefficient used for the hot top region ($10 \text{ W m}^{-2} \text{ K}^{-1}$)

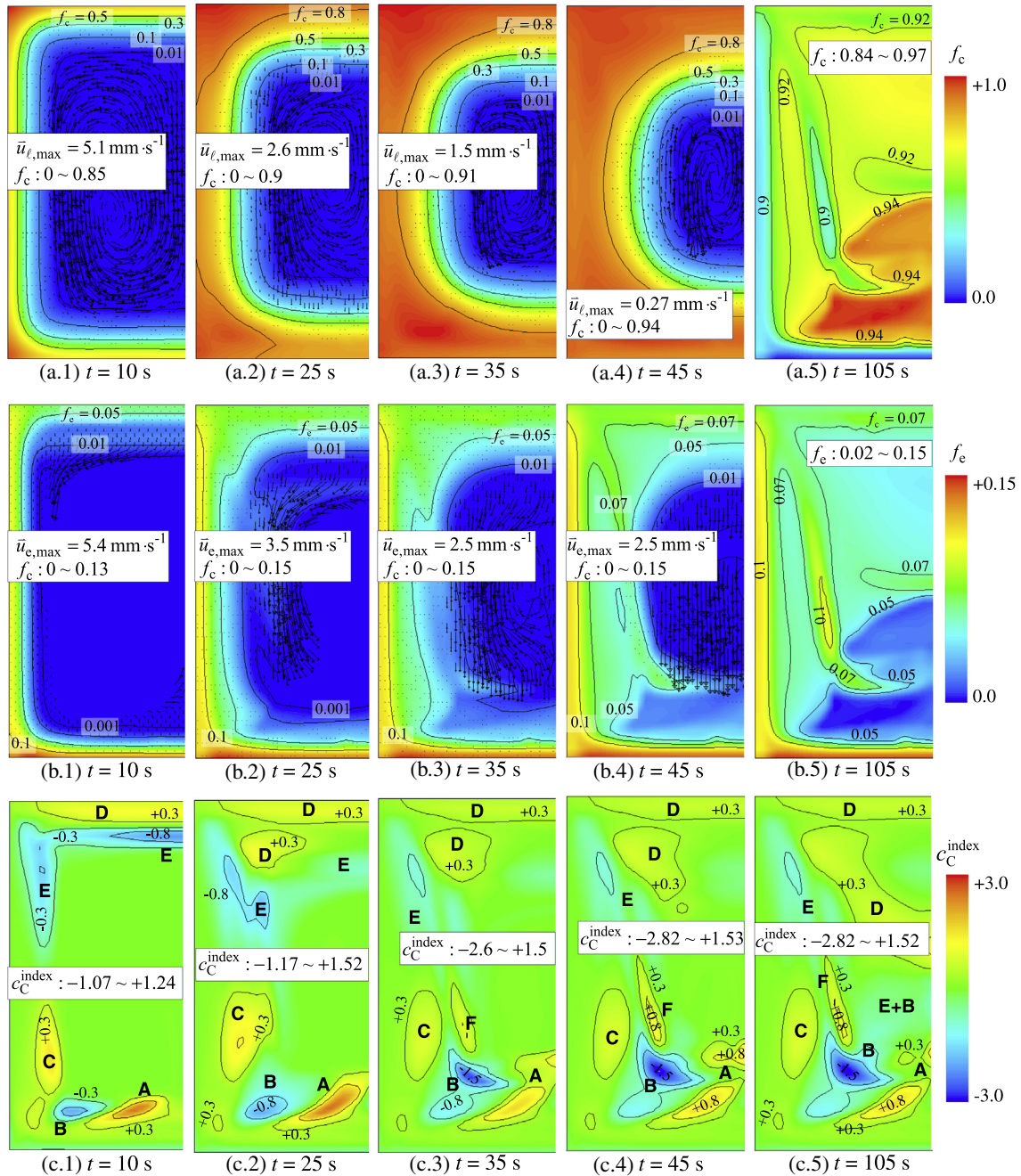


Fig. 13. Solidification sequence and evolution of macrosegregation during mixed columnar–equiaxed solidification. The results are presented for the case Mix-1, and finite diffusion growth kinetics is considered. \vec{u}_l and \vec{u}_e are shown in vectors, (a) and (b), overlaid with f_c and f_e -isolines. Only macrosegregation of C, c_C^{index} , is shown in both the color scale and their isolines (c). The different segregation zones are marked with the symbols A–E. (For interpretation of the references to colour in this figure legend, the reader is referred to the web version of this article.)

could be too small. The position of the predicted hot spot of this ingot appears too high compared with the one observed experimentally. However, we do not adjust the process parameters to cater to the experimental results in this study.

7. Discussion

7.1. Importance of finite diffusion kinetics in the formation of macrosegregation

Due to finite diffusion, the liquid average concentration is different from the thermodynamic equilibrium concentration, i.e. $c_{\ell,i} \neq c_{\ell,i}^*$. The deviation of $c_{\ell,i}$ from $c_{\ell,i}^*$, depending on the cooling

rate and diffusion length, is most significant at the initial stage of solidification [1]. At this stage, the crystal is mostly globular (equiaxed) or cellular (columnar), and the solute field around the crystal does not impinge on those of other neighboring crystals. The melt of concentration $c_{\ell,i}$, not $c_{\ell,i}^*$, is transported and governs the formation of macrosegregation. The flow in the inter-columnar or intergranular space is easier, and it is precisely at this early stage of solidification that the melt cannot be treated as infinite mixing. Therefore, a proper treatment of the diffusion kinetics of the liquid phase becomes critical for the calculation of macrosegregation. It is understandable that the assumption of $c_{\ell,i} = c_{\ell,i}^*$, imposed by the infinite mixing models (Gulliver–Scheil or lever rule), would lead to error estimation of macrosegregation.

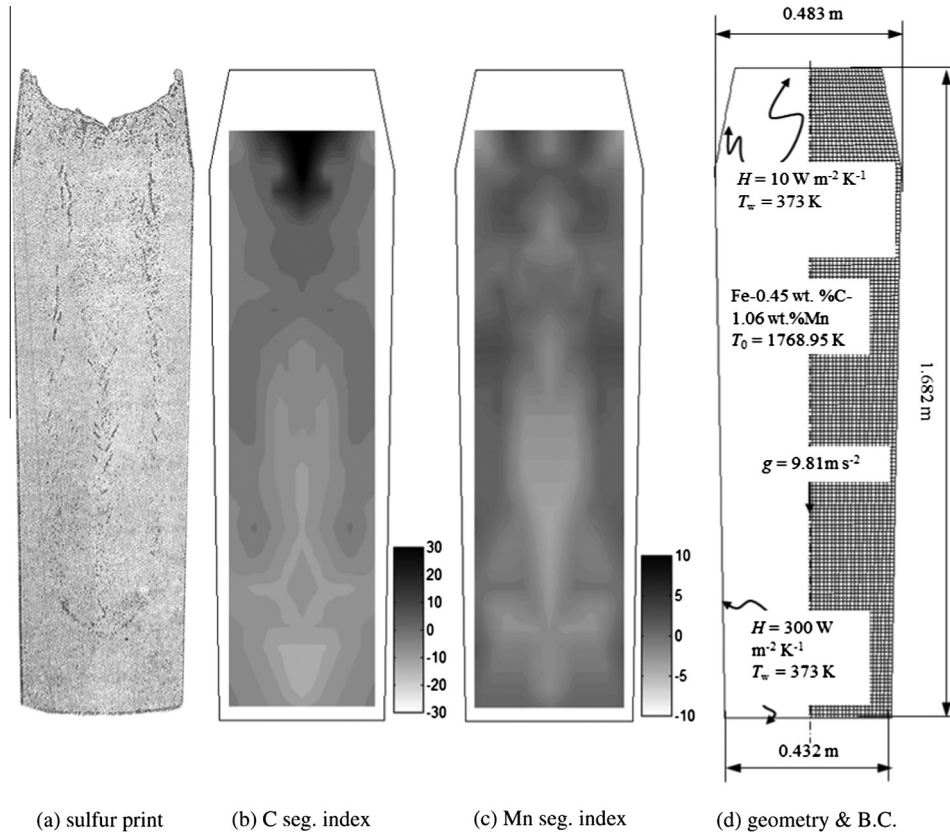


Fig. 14. Configuration of a 2.45-ton industry ingot (Fe-0.45 wt.%C-1.06 wt.%Mn). (a)–(c) Experimental results in accordance with [52] and (d) simulation setup. The reported macrosegregation is indicated by the segregation index $100 \times (c_{\text{mix},i} - c_{o,i}) / c_{o,i}$ in grayscale.

One may argue that the infinite mixing does give a reasonable approximation at the late stage of solidification. However, the flow can be ignored at the late stage and almost stops at a solid fraction of approximately 0.3 for columnar solidification (Fig. 3(a)) or at approximately 0.5 for equiaxed solidification (Fig. 8(a)). The resistance of the columnar crystals to the flow is proportional to f_c^2 / f_l [43], and the drag force of the settling equiaxed crystals to the surrounding melt is proportional to $f_e^{4/3} / f_l$ [29]. This result means that the (treatment of) solute enrichment in the interdendritic melt in the late stage of solidification does not significantly affect the calculation of the macrosegregation.

Another important point worth mentioning here is the invalidity of the infinite mixing models for calculation of the mixed columnar–equiaxed solidification and the columnar-to-equiaxed transition. A necessary feature of the mixed columnar–equiaxed solidification model is to consider the competition between the growth of the columnar primary dendrite tips and the equiaxed crystals ahead. As shown in Fig. 5, if the columnar primary dendrite tip front is tracked, for example, using the LGK model [2,43,48], in combination with the infinite mixing growth kinetics (Gulliver–Scheil or lever rule), a ‘cut’ $T-f_c$ curve and a narrow mushy zone are predicted, especially in the region between $f_c = 0$ and 0.3, where interdendritic flow is relatively easier. This phenomenon will significantly affect the flow pattern in the columnar primary dendrite tip region and consequently affect the result of macrosegregation.

During columnar or mixed columnar–equiaxed solidification, meso-segregation (channel segregation) might occur; however, the imposed infinite mixing in the liquid phase by Gulliver–Scheil or the lever rule leads to an overestimation of the meso-segregation. The reason has been discussed by Zaloznik and Combeau [30]. Consideration of finite diffusion in the liquid phase indicates stabilization of the growth of the mushy zone. Due to this

increased stability, the sensitivity of the phase-change to local solutal and flow perturbations is decreased, which inhibits the development of channels and thus the formation of meso-segregation. Similar analyses, which were performed previously by the authors [53–56], will not be repeated here.

C in both the liquid and solid has a larger diffusion coefficient than Mn. The current model shows that, independent from the assumed crystal morphology (columnar, equiaxed, or mixed columnar–equiaxed solidification), C is more prone to macrosegregation. We find that it is the partition coefficient ($k_C = 0.36$, $k_{Mn} = 0.75$) together with the relative velocity between the liquid and solid that govern the formation of macrosegregation. The diffusion coefficients can only level out the difference between average and equilibrium concentrations in each phase. The difference between concentrations of liquid and solid is mainly governed by the partition coefficients and is less affected by the diffusion coefficients. Additionally, we have considered two possible partition mechanisms at the liquid–solid interface: the equilibrium mechanism and the non-equilibrium mechanism with solute trapping. The liquid diffusion coefficient of Mn is 1/5 that of C. The solute-trapping phenomenon is predicted for Mn at the initial stage of high cooling rate near the casting surface region. For C, no solute trapping occurs (only equilibrium partition). This modeling result hints that the low diffusive element increases the possibility of solute trapping.

Some uncertain points regarding the calculation of the diffusion length need to be improved in the future: (i) the effect of a moving liquid–solid interface, (ii) the transient behavior of growth, and (iii) the effect of flow. We have described in Part 1 [1] that the diffusion lengths are estimated based on the analytical solution of diffusion fields around and inside a stationary sphere or cylinder, which might have overestimated the diffusion length or overestimated

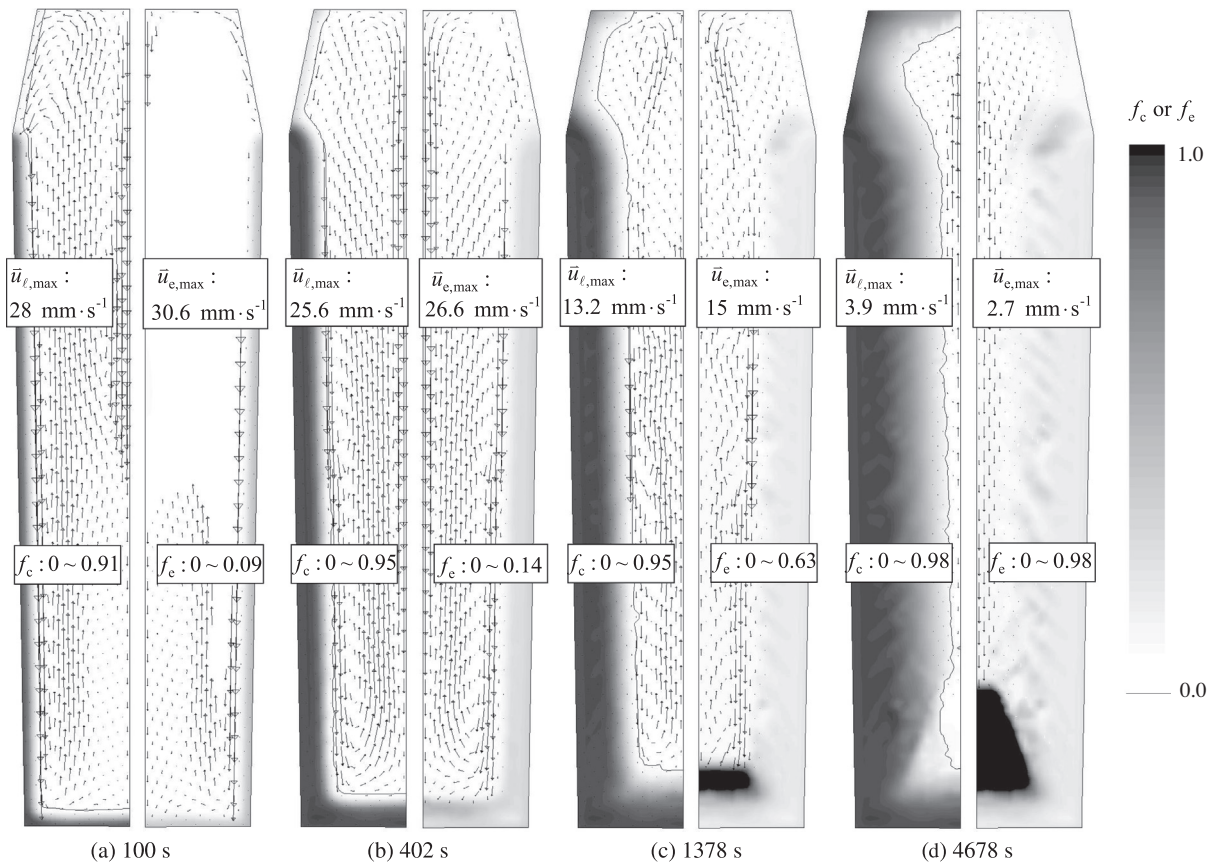


Fig. 15. Solidification sequence of the 2.45-ton ingot. The volume fraction of each phase (f_c or f_e) is shown in grayscale from the minimum (bright) to maximum (dark). The left half of each figure shows the evolution of f_c together with \bar{u}_l . The right half shows the evolution of f_e together with \bar{u}_e . The columnar dendrite tip position is also marked with a solid black line.

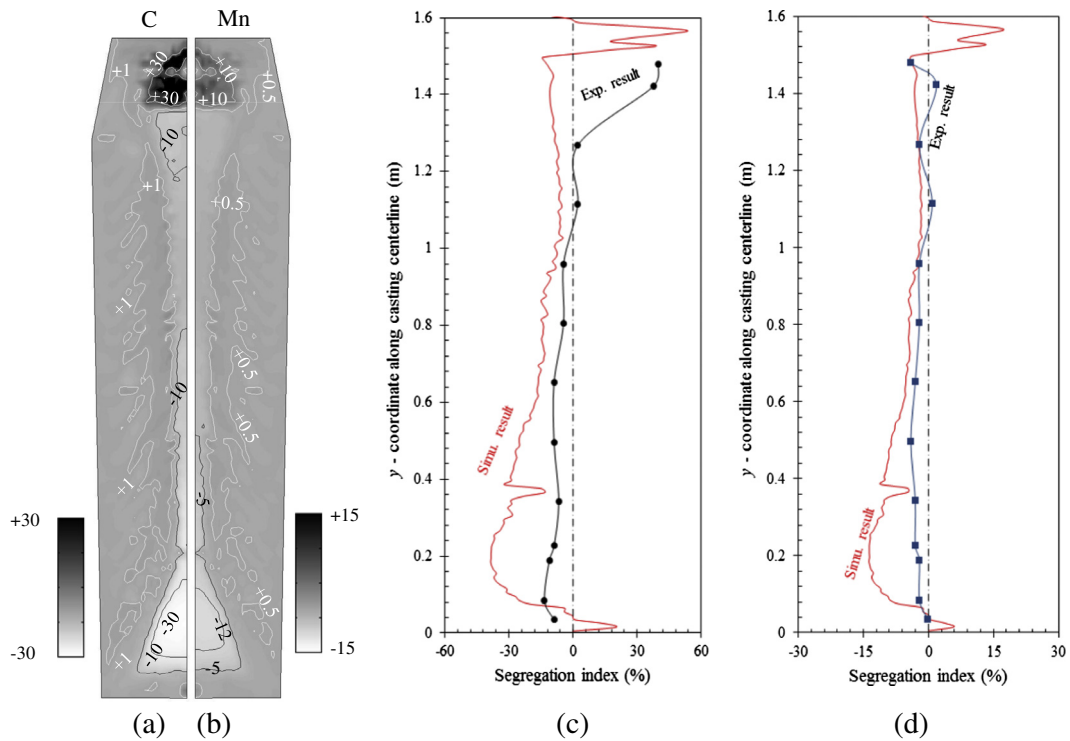


Fig. 16. Numerically predicted macrosegregation map, c_i^{index} : (a) C, (b) Mn, (c) segregation of C along the centerline, and (d) segregation of Mn along the centerline compared with experimental results.

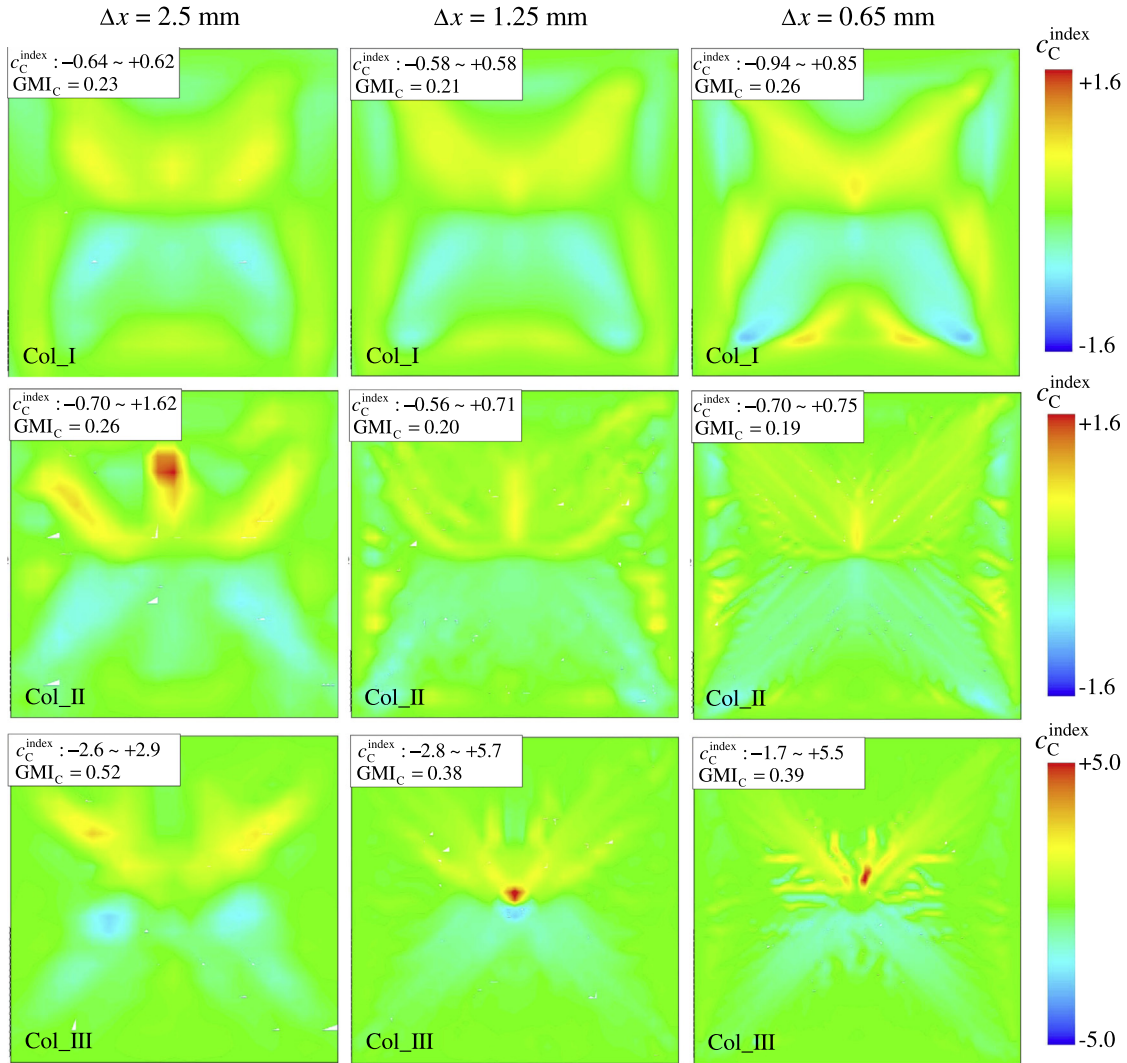


Fig. 17. Sensitivity of the predicted macrosegregation pattern to the mesh size (2.5, 1.25 and 0.65 mm). Three pure columnar solidification cases considering different diffusion kinetics are compared. Only the segregation of C is evaluated. The local macrosegregation index distribution range ($c_{C,\min}^{\text{index}} \sim c_{C,\max}^{\text{index}}$) and the global macrosegregation intensity (GMI_C) are labeled in each calculation.

the possibility of solute trapping. For point (i), a possible improvement of the diffusion length by accounting for the motion of a growing liquid–solid interface can be performed [33]. For point (ii), a numerical solution of the transient diffusion field in and around the growing liquid–solid interface can be used to calculate the varying diffusion length [57]. However, both of the above improvements would lead to a high calculation cost, as a numerical integration or solution of the local diffusion field in and around the growing crystal must be performed on the base of each computational volume element, iteration and time step. For point (iii) a modification to the diffusion length due to flow can be performed by introducing a Sherwood number (the diffusion length is related to the grain size, Reynolds and Schmidt numbers) [58]. The Sherwood number determined experimentally based on an organic material must be further validated for a metallic alloy.

7.2. Mesh sensitivity

Mesh size is an important factor that affects the accuracy of macrosegregation calculations. The model was implemented in commercial software, ANSYS Fluent [43,59]. The calculation accuracy is controlled by the residual, which is the sum of the

imbalance in the discretized conservation equations over all cells, $\sum_{\text{cells}, p} | \sum_{\text{nb}} a_{\text{nb}} \phi_{\text{nb}} + b - a_p \phi_p |$, normalized by a scaling factor, $\sum_{\text{cells}, p} | a_p \phi_p |$. Here, ϕ_p and ϕ_{nb} are values of a general variable ϕ at a cell p and neighbor cells nb , a_p is the center coefficient, a_{nb} represent the effect coefficients for the neighboring cells, and b is the contribution of the constant part of the source term. Convergence criteria were strictly controlled: the normalized residuals for continuity, momentum, volume fraction, species transport and user-defined scalar equations were set to 10^{-4} , and for enthalpy conservation equations, the residuals were set to 10^{-7} . To fulfill the above criteria, the time step had to be set as small as 10^{-4} s for some cases of fine grid, and the maximum iterations per time step was set to 60.

Mesh sensitivity was studied for the 2D square casting (Figs. 17 and 18). For the pure columnar solidification, the sensibility of the calculation results to the mesh size also depends on the assumed diffusion kinetics (Fig. 17). With finite diffusion kinetics (Col-I), the global macrosegregation pattern does not change so much when the mesh size is smaller than 1.25 mm; however, the segregation strength is still not convergent with a grid size of 0.65 mm. Here, the segregation strength is evaluated by the GMI_C and the positive and negative segregation extremes ($c_{C,\min}^{\text{index}}$). With the

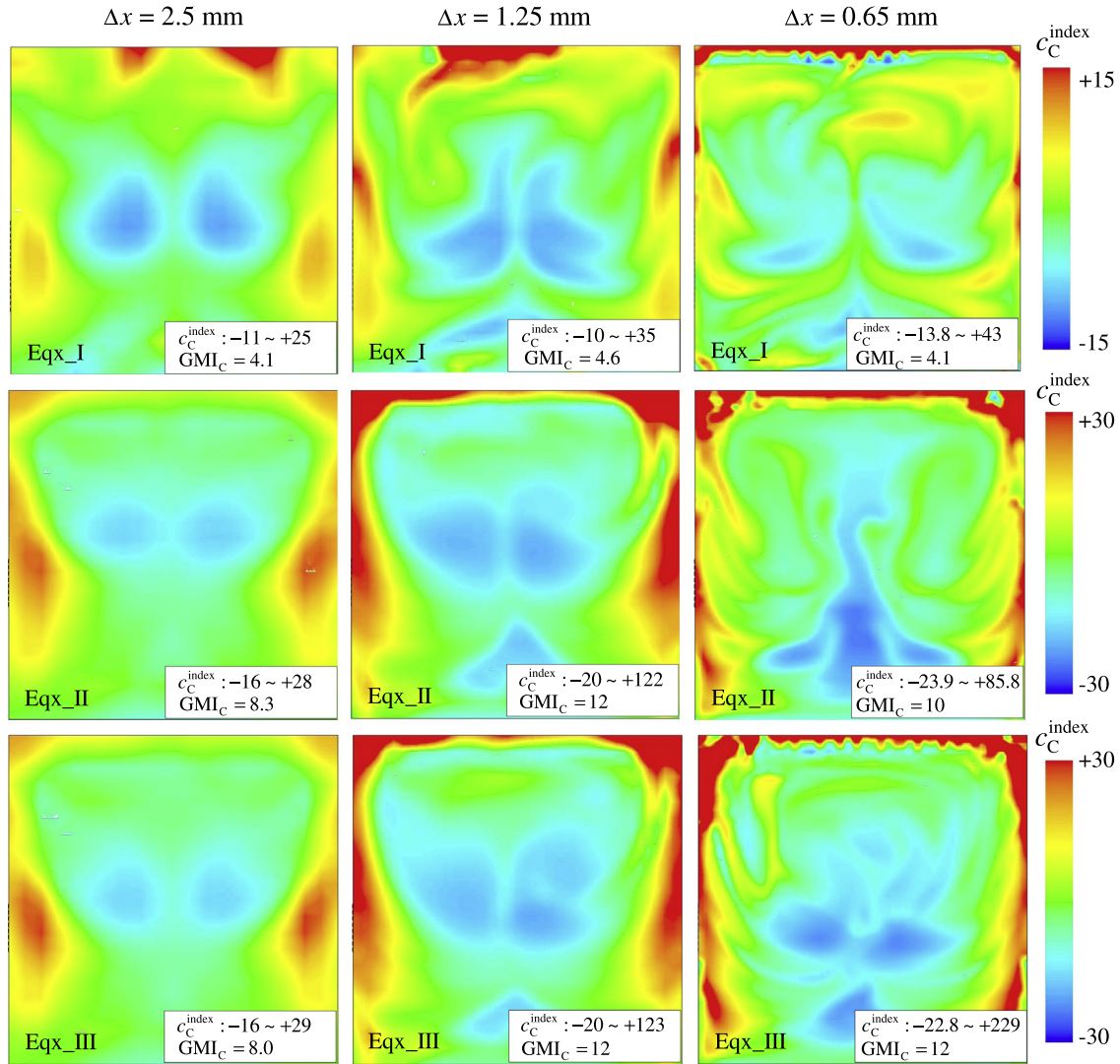


Fig. 18. Sensitivity of the predicted macrosegregation pattern to the mesh size (2.5, 1.25 and 0.65 mm). Three pure equiaxed solidification cases considering different diffusion kinetics are compared. Only the segregation of C is evaluated. The local macrosegregation index distribution range ($c_{C,\min}^{\text{index}} \sim c_{C,\max}^{\text{index}}$) and the global macrosegregation intensity (GMI_C) are labeled in each calculation.

infinite liquid mixing kinetics (Col-II and Col-III), both the global macrosegregation pattern and the segregation strength are extremely sensitive to the grid size. Meso-segregation (channel segregation) is predicted with a grid size smaller than 1.25 mm, while no such pattern is observed with a coarse grid (2.5 mm). To conclude this discussion, the model with the assumption of infinite liquid mixing is more sensitive to the grid resolution than the model considering finite diffusion kinetics for similar reasons to those discussed in Section 7.1. The assumption of infinite liquid mixing leads to an overestimation of meso-segregation; however, this meso-segregation cannot be properly resolved with a coarse grid (2.5 mm).

For pure equiaxed solidification, as the velocity of the flow/sedimentation is one order of magnitude larger than that for the cases of pure columnar solidification, the modeling result shows much more sensitivity to the mesh size. Even if the finite diffusion kinetics is considered, the segregation pattern and the segregation strength are not fully convergent. As shown in Fig. 18, none of the 3 cases (Eqx-I, Eqx-II, Eqx-III) is convergent with a grid size of 0.65 mm. Calculations with finer grids demand even smaller time steps, and each calculation would require a few weeks, which currently prohibits a systematic study. Therefore, care must be taken to interpret the results of Section 4 (pure

equiaxed solidification), and the result can only lead to a qualitative conclusion.

A mesh sensitivity study of a 2.45-ton ingot casting with mixed columnar–equiaxed solidification was also made and presented elsewhere [54]. It was observed that a very fine grid was required to predict the details of quasi A-segregation (or A-segregates). A grid-independent result regarding the fine details of quasi A-segregation in such ingots is not attainable based on current calculations. However, the global segregation pattern, e.g., the positive segregation extreme, negative segregation extreme, and their locations, can be obtained using a relatively coarse grid (10 mm).

8. Conclusions

Simulations of a 2D square casting of a ternary alloy (Fe–0.45 wt.%–1.06 wt.%Mn) with flow and crystal sedimentation were performed. The importance of the proper handling of the finite diffusion kinetics in the calculation of macrosegregation was investigated.

- (1) By comparing different diffusion kinetics, we observed that the infinite mixing kinetics as assumed by the classical solidification model, e.g., Gulliver–Scheil or the lever rule, which

cannot properly consider the solute enrichment in the interdendritic or inter-granular melt at the early stage of solidification, might lead to an erroneous estimation of macrosegregation.

- (2) Crystal morphology is an important factor affecting the formation of macrosegregation. Pure equiaxed solidification leads to much more severe segregation than pure columnar solidification. The difference is large: the former case would produce one order of magnitude more severe segregation than the latter case. During mixed columnar–equiaxed solidification, the appearance of a columnar structure significantly reduces the flow and crystal sedimentation, hence reducing the macrosegregation.
- (3) Both Gulliver–Scheil and the lever rule overestimate mesosegregation, i.e., the channel segregation. This statement requires further experimental verification; however, the same conclusion was drawn by Zaloznik and Combeau based on their numerical study [30].
- (4) Mesh size is an important factor affecting the calculation accuracy of macrosegregation. However, the issue of mesh sensitivity also depends on diffusion kinetics. If finite diffusion kinetics applies, a grid-independent result is easier to obtain. If infinite diffusion kinetics applies, the modeling result is more sensitive to the grid resolution. It must be stated that although quantitative parameter studies have been performed, conclusions can only be drawn qualitatively, as the calculations of some cases are not fully convergent with the finest grid (0.65 mm) used in this paper.

Summarizing the modeling results of this two-part investigation (Part-1 and Part-2), the model that accounts for finite diffusion kinetics is highly recommended for the calculation of both micro- and macrosegregation.

The simulation of macrosegregation in an engineering steel ingot of 2.45 tons is illustrated, and the simulation results are compared with experimental results. The key features of the macrosegregation in this ingot were verified to be numerically reproducible; however, the quantitative discrepancy remains large. Further investigations are suggested: first, to continue the model evaluation with engineering ingots with more reliable process conditions and parameters and, second, to enhance the model capacity by considering an improved model for diffusion lengths and dendritic morphology.

Acknowledgments

This work was financially supported by the FWF Austrian Science Fund (P23155-N24), the Austrian Federal Ministry of Economy, Family and Youth and the National Foundation for Research, Technology and Development within the framework of the Christian-Doppler Laboratory for Advanced Process Simulation of Solidification and Melting.

References

- [1] M. Wu, J. Li, A. Ludwig, A. Kharicha, *Comp. Mater. Sci.* 79 (2013) 830–840.
- [2] W. Kurz, D.J. Fisher, *Fundamentals of Solidification*, Trans. Tech. Publication, Switzerland, 1998, pp. 280–288.

- [3] H.D. Brody, M.C. Flemings, *Trans. Metall. Soc. AIME* 236 (1966) 615–625.
- [4] T.W. Clyne, W. Kurz, *Metall. Trans.* 12A (1981) 965–971.
- [5] M. Rappaz, Ph. Thévoz, *Acta Metall.* 35 (1987) 1487–1497.
- [6] M. Rappaz, Ph. Thévoz, *Acta Metall.* 35 (1987) 2929–2933.
- [7] M. Rappaz, W.J. Boettinger, *Acta Mater.* 47 (1999) 3205–3219.
- [8] M.C. Flemings, *ISIJ Int.* 40 (2000) 833–841.
- [9] C. Beckermann, *Int. Mater. Rev.* 47 (2002) 234–261.
- [10] W.D. Bennon, F.P. Incropera, *Int. J. Heat Mass Trans.* 30 (1987) 2161–2170.
- [11] W.D. Bennon, F.P. Incropera, *Int. J. Heat Mass Trans.* 30 (1987) 2171–2187.
- [12] M.J.M. Krane, F.P. Incropera, D.R. Gaskell, *Int. J. Heat Mass Trans.* 40 (1997) 3827–3835.
- [13] M.J.M. Krane, F.P. Incropera, *Int. J. Heat Mass Trans.* 40 (1997) 3837–3847.
- [14] N. Ahmad, H. Combeau, J.L. Desbiolles, T. Jalanti, G. Lesoult, J. Rappaz, M. Rappaz, C. Stomp, *Metall. Mater. Trans.* 29A (1998) 617–630.
- [15] M. Schneider, C. Beckermann, *Int. J. Heat Mass Trans.* 38 (1995) 3455–3473.
- [16] V.R. Voller, A.D. Brent, C. Prakash, *Int. J. Heat Mass Trans.* 32 (1989) 1719–1731.
- [17] Q. Du, D.G. Eskin, L. Katgerman, *Metall. Mater. Trans.* 38A (2007) 180–189.
- [18] M. Schneider, C. Beckermann, *Metall. Mater. Trans.* 26A (1995) 2373–2388.
- [19] J.P. Gu, C. Beckermann, *Metall. Mater. Trans.* A 30A (1999) 1357–1366.
- [20] M. Rappaz, V. Voller, *Metall. Trans.* A 21A (1990) 749–753.
- [21] X. Dore, H. Combeau, M. Rappaz, *Acta Mater.* 48 (2000) 3951–3962.
- [22] L. Thuinet, H. Combeau, *J. Mater. Sci.* 39 (2004) 7213–7219.
- [23] M. Flemings, G.E. Nereo G-E, *Trans. Metall. Soc. AIME* 239 (1967) 1449–1461.
- [24] V.R. Voller, C. Beckermann, *Metall. Mater. Trans.* 30A (1999) 2183–2189.
- [25] H.J. Thevik, A. Mo, *Int. J. Heat Mass Trans.* 40 (1997) 2055–2065.
- [26] H.J. Thevik, A. Mo, T. Rusten, *Metall. Mater. Trans.* B 30B (1999) 135–142.
- [27] H.J. Thevik, A. Mo, *Metall. Mater. Trans.* B 28B (1997) 665–669.
- [28] S. Sundarraj, V.R. Voller, *ASME Transport Phenomena in Solidification HTD-284* (1994) 29–42.
- [29] M. Wu, A. Ludwig, A. Bührig-Polaczek, M. Fehlbier, P.R. Sahm, *J. Heat Mass Trans.* 46 (2003) 2819–2832.
- [30] M. Zaloznik, H. Combeau, in: S. Cockcroft, D. Majer (Eds.), *Modeling of Casting, Welding and Advanced Solidification Processes XII*, TMS, Warrendale, PA, 2009, pp. 253–260.
- [31] J. Ni, C. Beckermann, *Metall. Trans.* 22B (1991) 349–361.
- [32] C. Beckermann, R. Viskanta, *Appl. Mech. Rev.* 46 (1993) 1–27.
- [33] C.Y. Wang, C. Beckermann, *Metall. Trans.* 24A (1993) 2787–2802.
- [34] C.Y. Wang, C. Beckermann, *Mater. Sci. Eng.* 171A (1993) 199–211.
- [35] C.Y. Wang, C. Beckermann, *Metall. Trans.* 27A (1996) 2754–2764.
- [36] A.I. Ciobanas, Y. Fautrelle, *J. Phys. D: Appl. Phys.* 40 (2007) 3733–3762.
- [37] A.I. Ciobanas, Y. Fautrelle, *J. Phys. D: Appl. Phys.* 40 (2007) 4310–4336.
- [38] M. Wu, A. Ludwig, *Acta Mater.* 57 (2009) 5621–5631.
- [39] M. Wu, A. Ludwig, *Acta Mater.* 57 (2009) 5632–5644.
- [40] M. Wu, A. Fjeld, A. Ludwig, *Comp. Mater. Sci.* 50 (2010) 32–42.
- [41] M. Wu, A. Ludwig, A. Fjeld, *Comp. Mater. Sci.* 50 (2010) 43–58.
- [42] M. Ahmadein, M. Wu, J.H. Li, P. Schumacher, A. Ludwig, *Metall. Mater. Trans.* 44A (2013) 2895–2903.
- [43] M. Wu, A. Ludwig, *Metall. Mater. Trans.* 37A (2006) 1613–1631.
- [44] M. Wu, A. Ludwig, *Metall. Mater. Trans.* 38A (2007) 1465–1475.
- [45] A. Ludwig, M. Gruber-Pretzler, F. Mayer, A. Ishmurzin, M. Wu, *Mater. Sci. Eng. A* 413–414 (2005) 485–489.
- [46] A. Ishmurzin, M. Gruber-Pretzler, F. Mayer, M. Wu, A. Ludwig, *Int. J. Mat. Res.* 99 (2008) 618–625.
- [47] W. Oldfield, *Trans. ASM* 59 (1966) 945–961.
- [48] J. Lipton, M.E. Glicksman, W. Kurz, *Mater. Sci. Eng.* 65 (1984) 57–63.
- [49] P.K. Galenko, D.A. Danilov, *J. Cryst. Growth* 197 (1999) 992–1002.
- [50] M. Wu, L. Könözy, A. Ludwig, W. Schützenhofer, R. Tanzer, *Steel Res. Int.* 79 (2008) 637–644.
- [51] M. Wu, A. Ludwig, J. Luo, *Mater. Sci. Forum.* 475–479 (2005) 2725–2730.
- [52] J. Iron Steel Institute, Report on the heterogeneity of steel ingots 103 (1926) 39–176.
- [53] J. Li, M. Wu, A. Ludwig, A. Kharicha, *IOP Conf. Series: Mater. Sci. Eng.* 33 (2012), <http://dx.doi.org/10.1088/1757-899X/33/1/012091>.
- [54] J. Li, M. Wu, A. Ludwig, A. Kharicha, *Int. J. Heat Mas Trans.* 72 (2014) 668–679.
- [55] J. Li, M. Wu, J. Hao, A. Ludwig, *Comp. Mater. Sci.* 55 (2012) 407–418.
- [56] J. Li, M. Wu, J. Hao, A. Kharicha, A. Ludwig, *Comp. Mater. Sci.* 55 (2012) 419–429.
- [57] L. Thuinet, H. Combeau, *Comp. Mater. Sci.* 45 (2009) 294–304.
- [58] A. Badillo, D. Ceynar, C. Beckermann, *J. Cryst. Growth* 309 (2007) 197–215.
- [59] ANSYS Fluent – Release 14.5, *Fluent Theory Guide*, ANSYS Inc, <www.ansys.com>.